# A Systematic Relationship between the Representations of Convectively Coupled Equatorial Wave Activity and the Madden–Julian Oscillation in Climate Model Simulations

YANJUAN GUO

*Joint Institute for Regional Earth System Science and Engineering, University of California, Los Angeles, Los Angeles, California*

DUANE E. WALISER

*Joint Institute for Regional Earth System Science and Engineering, University of California, Los Angeles, Los Angeles, and Jet Propulsion Laboratory, California Institute of Technology, Pasadena, California*

XIANAN JIANG

*Joint Institute for Regional Earth System Science and Engineering, University of California, Los Angeles, Los Angeles, California*

(Manuscript received 10 July 2014, in final form 20 November 2014)

ABSTRACT

The relationship between a model's performance in simulating the Madden–Julian oscillation (MJO) and convectively coupled equatorial wave (CCEW) activity during wintertime is examined by analyzing precipitation from 26 general circulation models (GCMs) participating in the MJO Task Force/Global Energy and Water Cycle Experiment (GEWEX) Atmospheric System Study (GASS) MJO model intercomparison project as well as observations based on the Tropical Rainfall Measuring Mission (TRMM). A model's performance in simulating the MJO is determined by how faithfully it reproduces the eastward propagation of the large-scale intraseasonal variability (ISV) compared to TRMM observations. Results suggest that models that simulate a better MJO tend to 1) have higher fractional variances for various high-frequency wave modes (Kelvin, mixed Rossby–gravity, and westward and eastward inertio-gravity waves), which are defined by the ratios of wave variances of specific wave modes to the "total" variance, and 2) exhibit stronger CCEW variances in association with the eastward-propagating ISV precipitation anomalies for these high-frequency wave modes. The former result is illustrative of an alleviation in the good MJO models of the widely reported GCM deficiency in simulating the correct distribution of variance in tropical convection [i.e., typically too weak (strong) variance in the high- (low-) frequency spectrum of the precipitation]. The latter suggests better coherence and stronger interactions between these aforementioned high-frequency CCEWs and the ISV envelope in good MJO models. Both factors likely contribute to the improved simulation of the MJO in a GCM.

## 1. Introduction

Tropical convection is known to be organized over a wide range of spatial and temporal scales, from mesoscale convective systems (Houze 2004) to convectively coupled equatorial waves (CCEWs; Kiladis et al. 2009) and to the planetary-scale Madden–Julian oscillation (MJO; Madden and Julian 1971, 1972). In this study, we will focus on the latter two categories that are explicitly resolved by general circulation models (GCMs).

The MJO is the dominant mode of tropical intraseasonal (30–90 day) variability (ISV), which is characterized by planetary-scale ($\sim 10^4$ km), slowly eastward-propagating ($\sim 5\,\mathrm{m\,s^{-1}}$) convection anomalies that prevail over the equatorial Indian Ocean and western Pacific Ocean (e.g., Zhang 2005; Wang 2005). The CCEWs include Kelvin, equatorial Rossby (ER), mixed Rossby–gravity (MRG), eastward inertio-gravity (EIG), and westward inertio-gravity (WIG) waves (Takayabu 1994; Wheeler and

*Corresponding author address:* Dr. Yanjuan Guo, Jet Propulsion Laboratory, M/S 233-304, 4800 Oak Grove Dr., Pasadena, CA 91109.
E-mail: yguo@jifresse.ucla.edu

DOI: 10.1175/JCLI-D-14-00485.1

Kiladis 1999, hereafter WK99; Kiladis et al. 2009), which correspond to the solutions of the shallow water model (Matsuno 1966) with a modified equivalent depth (WK99). The CCEWs can move eastward or westward, either along the equator or within a few degrees of latitude parallel to it. Among them, Kelvin, MRG, EIG and WIG waves have typical period of days and spatial scales of $10^3$ km and, thus, are referred to as tropical synoptic waves in some literatures (e.g., Khouider et al. 2012). The ER waves are relatively slower and have comparable temporal and spatial scales compared to the MJO (WK99; Kiladis et al. 2009). The MJO and the CCEWs strongly affect the tropical weather and climate, which has been documented in a large number of previous studies (e.g., Lau and Waliser 2005; Zhang 2005; Wang 2005; WK99; Kiladis et al. 2009). In addition, they influence the midlatitude through various tropical–extratropical teleconnection patterns. Moreover, the MJO has been believed to be a key source of untapped predictability for the extended-range forecast in both the tropics and the extratropics (e.g., Schubert et al. 2002; Waliser et al. 2003; review in Waliser 2011). Because of this apparent importance, numerous studies have been carried out that examine different perspectives of the MJO and CCEW relationship. This study will focus on exploring possible relationships between the simulated MJO and CCEWs in climate models.

The MJO and the CCEWs are closely related to each other within the context of multiscale interaction. The pioneering work by Nakazawa (1988) using satellite observations showed that the MJO is a slowly eastward-propagating, planetary-scale envelope of embedded eastward-propagating convectively coupled Kelvin waves, which in turn appear as envelopes of westward-propagating 2-day waves (or WIG waves). The presence of the Kelvin wave as well as other types of CCEWs within the MJO convection complex was identified in many subsequent studies (Straub and Kiladis 2003; Haertel and Kiladis 2004; Moncrieff 2004; Kikuchi and Wang 2010; Zuluaga and Houze 2013). On one hand, the MJO exerts strong modulation on the CCEWs that form within it, primarily through its influence on the environmental moisture and circulation fields (Roundy and Frank 2004; Yang et al. 2007; Roundy 2008; Khouider and Majda 2008b; Khouider et al. 2012; Guo et al. 2014). On the other hand, the CCEWs feed back to the MJO through the upscale transports of momentum, temperature, and moisture (Hendon and Liebmann 1994; Houze et al. 2000; Moncrieff 2004; Masunaga et al. 2006; Wang and Liu 2011; Liu and Wang 2012). These two-way interactions between the MJO and the CCEWs are regarded as one of the fundamental features of the MJO, and form the basis of the so-called multiscale models that had been developed to study the roles of the scale interaction in the MJO (Majda and Klein 2003; Majda and Biello 2004; Biello and Majda 2005; Majda and Stechmann 2009; Wang and Liu 2011; Liu and Wang 2012).

Despite the attempts of many theoretical and simplified modeling studies to explain the physics behind the MJO as well as its multiscale interactions with the CCEWs, the simulation of the MJO and CCEWs in GCMs has proven to be a difficult task for decades (Slingo et al. 1996; Waliser et al. 2003; Lin et al. 2006; Zhang et al. 2006; Sperber and Annamalai 2008; Yang et al. 2009; Kim et al. 2009; Straub et al. 2010; Kim et al. 2011; Weaver et al. 2011; Sperber et al. 2008; Huang et al. 2013; Hung et al. 2013). For example, Slingo et al. (1996) examined models that were included in the Atmospheric Model Intercomparison Project (AMIP) and found that none of the models captured the dominance of the MJO in space–time spectral analysis identified in the observations. Lin et al. (2006) examined 14 GCMs that were included in phase 3 of the Coupled Model Intercomparison Project (CMIP3), and found that only two models in CMIP3 have MJO variance comparable to that observed, and even those two lack realism in many other MJO features. In terms of the CCEWs, only about half of the 14 CMIP3 GCMs examined by Lin et al. (2006) have prominent signals of CCEWs, and the variances of the simulated CCEWs, except the eastward inertio-gravity and Kelvin waves, are generally weaker compared to the observations. Yang et al. (2009) also showed that the simulated CCEWs in the Hadley Centre climate models are deficient. Straub et al. (2010) further investigated the CCEWs in 20 CMIP3 coupled GCMs, and found that only a few models can simulate the Kelvin wave with a realistic activity distribution and spatial structure. As an update to the study by Lin et al. (2006), Hung et al. (2013) examined 20 models from phase 5 of CMIP (CMIP5) and found that CMIP5 models generally produce larger variances of MJO, Kelvin, ER, and EIG waves compared to those in CMIP3. But there are still very few models that are able to simulate realistic eastward propagation of the MJO. Challenges for faithfully simulating the MJO and the CCEWs are related to model issues concerning the convective parameterization [see a brief summary in the introduction of Hung et al. (2013)], boundary layer parameterization, cloud microphysics, etc.

As efforts toward improving the MJO performance in GCMs are continuously required, the Working Group on Numerical Experimentation (WGNE) MJO Task Force (MJOTF) and Global Energy and Water Cycle Experiment (GEWEX) Atmospheric System Study (GASS) have recently combined forces under the auspices of Year of Tropical Convection (YOTC; Moncrieff et al. 2012;

Waliser et al. 2012) to organize a model intercomparison project to improve our understanding of the MJO (the MJOTF/GASS project), particularly focusing on the essential roles and vertical structure of diabatic heating and related moist processes in MJO physics (Petch et al. 2011). This MJO model intercomparison project consists of three experimental components, including (i) a 20-yr climate simulation, (ii) a 20-day hindcast, and (iii) a 2-day hindcast component. Comprehensive results based on each component are being first reported in three research papers, respectively (Jiang et al. 2015; Xavier et al. 2015; Klingaman et al. 2015).

In this study, we will make use of the outputs from 26 models that contributed to the 20-yr climate simulation component of this project. Precipitation data over the 20-yr period are used to examine the general behavior of the MJO and the CCEW activity in the model simulations. Our focus will be on exploring the possible relationships between a model's performance in simulating the MJO and its simulation of the CCEW activity across a large number of GCM simulations, which has not been examined before. Previous multimodel studies usually evaluated the performance of the MJO and the CCEWs separately, with little emphasis on the linkage between these two. One possible reason is that most GCMs are unable to simulate a realistic MJO (Lin et al. 2006; Hung et al. 2013), so there is a lack of basis to further examine its relationship to the higher-frequency CCEWs. However, as will be shown in this study, about a quarter of the models that participated in the MJOTF/GASS project show reasonable simulations of the MJO, making the current study feasible.

The rest of this paper is organized as follows. Section 2 describes the data and methodology used in this paper, including the identification of the ISV (as a measure of the MJO) and the CCEWs, and the approach to scoring a model's MJO performance. Section 3 discusses the climatology of the ISV and CCEW activity, as well as possible relationships between the strength of the CCEW variance and the MJO performance across all the models. In section 4, we will examine the variations of the CCEW activity associated with the ISV variation, and the implication of this CCEW–ISV interaction for the MJO simulation. Finally, discussions and conclusions are presented in section 5.

## 2. Data and methodology

### a. Data

In this study, precipitation, which is indicative of the large-scale convective signal, is the only meteorological variable used. Precipitation data are examined for both GCM simulations and observation.

Table 1 lists the 26 models examined in this study that participated in the MJOTF/GASS MJO model intercomparison project. These model simulations are either with an atmosphere-only GCM (AGCM) or based on an atmosphere–ocean coupled system (denoted by an asterisk). More details can be found at the project website (http://www.ucar.edu/yotc/mjodiab.html). Twenty-year daily precipitation data during 1991–2010 from each model have been regridded onto a common 2.5° × 2.5° latitude–longitude grid.

Observations of precipitation taken from the Tropical Rainfall Measuring Mission (TRMM) 3B42 version 7 dataset (Huffman et al. 2007) that have been interpolated onto the same temporal and horizontal resolution as the model simulations, are used to compare with the model outputs. The time period of the TRMM data is from 1998 to 2012.

This study focuses on the Northern Hemisphere extended winter season (November–April) when the traditionally defined MJO is most active and coincident with the near-equatorial region (e.g., Waliser 2006).

### b. WK-filtering method for extracting CCEW anomalies

To isolate the convection signals corresponding to the CCEWs, a zonal wavenumber–frequency filtering, or so-called WK filtering (WK99), is applied to the precipitation data. This is accomplished by retaining only those spectral coefficients corresponding to the spectral peaks associated with a specific mode in the wavenumber–frequency domain. The domains used to extract individual CCEWs are indicated in Table 2, which follow those defined by Kiladis et al. (2009). More details on the WK-filtering method can be found in WK99. Both symmetric and asymmetric components about the equator are retained for these CCEWs.

Prior to the WK filtering, the annual cycle (mean and the first three harmonics) of the precipitation was first removed from its daily time series to produce the anomalies at each grid point. These anomalies are called the total anomalies in this study since variability on all time scales is retained except for the annual cycle. These total anomalies are then used to carry out the WK filtering to produce the individual CCEW wave anomalies, namely ER, Kelvin, MRG, and WIG and EIG waves. In addition, a 20–100-day bandpass filtering is applied to obtain the ISV anomalies, which are used in this study to generally represent the model's MJO variability and, in particular, to provide a means of scoring the model's MJO performance (described later in section 2d). The winter variances of the individual wave modes based on TRMM precipitation data are shown in Fig. 1 to provide the climatological maps of the wave activity of these

TABLE 1. Participating models with horizontal and vertical resolutions and main references. Coupled GCM models are denoted with an asterisk. Spectral model horizontal resolutions are listed with their spectral wavenumber truncations (preceded by T for triangular and R for rhomboidal) and the associated Gaussian grid spacing in parentheses. [Adopted from Table 1 in Jiang et al. (2015).]

| | Model name | Institution | Horizontal resolution, vertical levels | Reference |
|---|---|---|---|---|
| 1 | NASAGMAO_GEOS5 | NASA Global Model and Assimilation Office, United States | 0.625° × 0.5°, L72 | Molod et al. (2012) |
| 2 | SPCCSM* | George Mason University, United States | T42 (2.8°), L30 | Stan et al. (2010) |
| 3 | GISS_ModelE2 | NASA Goddard Institute for Space Studies, United States | 2.75° × 2.2°, L40 | Schmidt et al. (2014) |
| 4 | EC_GEM | Environment Canada, Canada | 1.4°, L64 | Côté et al. (1998) |
| 5 | MIROC | Japan Agency for Marine–Earth Science and Technology, Japan | T85 (1.5°), L40 | Watanabe et al. (2010) |
| 6 | MRI-AGCM | Meteorological Research Institute, Japan | T159, L48 | Yukimoto et al. (2012) |
| 7 | CWB_GFS | Central Weather Bureau, Taiwan | T119 (1°), L40 | Liou et al. (1997) |
| 8 | PNU_CFSv1 | Pusan National University, South Korea | T62 (2°), L64 | Saha et al. (2006) |
| 9 | MPI_ECHAM6* | Max Planck Institute for Meteorology, Germany | T63 (2°), L47 | Stevens et al. (2013) |
| 10 | MetUM_GA3 | Met Office, United Kingdom | 1.875° × 1.25°, L85 | Walters et al. (2011) |
| 11 | NCAR_CAM5 | National Center for Atmospheric Research, United States | T42 (2.8°), L30 | Neale et al. (2012) |
| 12 | NRL_NAVGEMv1.0 | Naval Research Laboratory, United States | T359 (37 km), L42 | Hogan et al. (2014) |
| 13 | UCSD_CAM | Scripps Institute of Oceanography, United States | T42 (2.8°), L30 | Zhang and Mu (2005) |
| 14 | NCEP_CFSv2 | NOAA/NCEP/Climate Prediction Center, United States | T126 (1°), L64 | Saha et al. (2014) |
| 15a | CNRM_AM | Météo-France/Centre National de la Recherche Scientifique, France | T127 (1.4°), L31 | Voldoire et al. (2013) |
| 15b | CNRM_ACM | | | |
| 15c | CNRM_CM | | | |
| 16 | CCCma_CanCM4* | Canadian Centre for Climate Modelling and Analysis, Canada | T63 (1.9°), L35 | Merryfield et al. (2013) |
| 17 | BCCAGCM2.1 | Beijing Climate Center, China Meteorological Administration, China | T42 (2.8°), L26 | Wu et al. (2010) |
| 18 | FGOALS-s2 | Institute of Atmospheric Physics, Chinese Academy of Sciences, China | R42 (2.8° × 1.6°), L26 | Bao et al. (2013) |
| 19 | NCHU_ECHAM5* | Academia Sinica, National Chung Hsing University, Taiwan | T63 (2°), L31 | Tsuang et al. (2001) |
| 20 | TAMU_Modi-CAM4 | Texas A&M University, United States | 2.5° × 1.9°, L26 | Lappen and Schumacher (2012) |
| 21 | ACCESS | Centre for Australian Weather and Climate Research, Australia | 1.875° × 1.25°, L85 | Zhu et al. (2013) |
| 22 | ISUGCM | Iowa State University, United States | T42 (2.8°), L18 | Wu and Deng (2013) |
| 23 | LLNL_CAM5ZMMicro | Lawrence Livermore National Laboratory, United States | T42 (2.8°), L30 | Song and Zhang (2011) |
| 24 | SMHI_ecearth3 | Rossby Centre, Swedish Meteorological and Hydrological Institute, Sweden | T255 (80 km), L91 | Hazeleger et al. (2012) |

waves from the observational perspective. It can be seen that the observed precipitation variances are largely confined to the Indian Ocean and western Pacific warm pool region between 15°S and 15°N, and this will be our region of interest.

### c. *Linear regression analysis*

In this study, the linear regression technique is heavily used; thus, it is briefly described here. Assume that there are $n$ data points for the dependent variable $y$ and the explanatory variable $x$. The goal of the linear regression is to find a straight line that best fits the data points. With the least squares approach, the slope of the fitted line ($\beta$) is determined as the correlation between $y$ and $x$ corrected by the ratio of the standard deviations of $y$ and $x$:

$$\beta = r_{xy}\frac{s_y}{s_x}, \tag{1}$$

in which $r_{xy}$ is the correlation between $y$ and $x$ and $s_y$ and $s_x$ are the standard deviations of $y$ and $x$, respectively. The slope $\beta$ can be interpreted as the conditionally expected change in $y$ for a one-unit change in $x$, which is the quantity that will be examined later on.

TABLE 2. Names of individual wave modes (first row), the filtering methods used to extract them (second row), and number of GCM models with wave variance smaller than the TRMM observations for each of them (third row). For the wavenumber $k$ shown, a positive sign denotes eastward propagation, while a negative sign is for westward propagation. $h_e$ is the "equivalent depth."

| Wave mode | Total | ISV | ER | Kelvin | MRG | WIG | EIG |
|---|---|---|---|---|---|---|---|
| Filtering method | Removal of the first three harmonics of the seasonal cycle | 20–100 day | 30–96 day; $-10 < k < -1$; dispersion curves with $h_e$ of 8 and 100 m | 2.5–14 day; $1 < k < 14$; dispersion curves with $h_e$ of 8 and 50 m | $-7 < k < -1$; dispersion curves with $h_e$ of 12 and 50 m | $-10 < k < -1$; dispersion curves with $h_e$ of 25 and 50 m | $1 < k < 14$; dispersion curves with $h_e$ of 25 and 50 m |
| No. of models with weaker than observed variance | 19 | 16 | 14 | 22 | 21 | 25 | 24 |

In this study, the ISV anomaly is the explanatory variable $x$, and a time series of ISV anomalies work as an ISV index onto which other quantities ($y$) are regressed.

### d. Determination of the MJO performance of a GCM

In this study, a GCM's MJO performance is evaluated according to its ability in capturing the key characteristics of the MJO, the coherent large-scale eastward propagation of the ISV anomalies, which is revealed by the lag regression of the ISV anomalies against an ISV index at a reference point following the approach used by Jiang et al. (2015). To be specific, the daily time series of the equatorially averaged (10°S–10°N for Kelvin, MRG, WIG, and EIG waves; 15°S–15°N for ER waves) ISV anomalies during the multiyear period (winter season only) were regressed against an ISV index, which is defined as the ISV anomalies averaged over a small reference box. For example, 5°S–5°N, 75°–85°E is used for the Indian Ocean reference point. The regression was done at time lags from day −20 to day 20 to generate a Hovmöller-like diagram (Fig. 2). The systematic eastward propagation of precipitation associated with the observed MJO starting from the Indian Ocean and dissipating near the date line is clearly seen based on TRMM data (Fig. 2, top left panels outlined by a rectangle).

Note that in the above lag-regression procedure, we purposely used the ISV anomalies (thus the ISV index) instead of the MJO anomalies (and a formal MJO index) to avoid preconditioning the answer by only examining/extracting the large-scale eastward-propagating part of the ISV. The underlying argument is that the systematic eastward propagation of the ISV will emerge in the lag regression of the ISV plot in the observations as well as in the GCMs with reasonable MJO simulations since the MJO dominates the ISV in the real atmosphere. On the other hand, in models with a poor depiction of the MJO, which often means that the model simulates too strong westward-propagating features, examining the ISV anomalies rather than the MJO anomalies will not prematurely exclude these features, thus providing the means to discern the true quality of the GCMs' representation of the MJO.

It is found that about one-quarter of the models can capture this eastward-propagating MJO mode quite well (NCHU_ECHAM5-SIT, TAMU_modCAM4, GISS_ModelE2, CNRM_CM, SPCCSM, PNU_CFS, and MRI_AGCM; see Fig. 2), and a few more are able to simulate the eastward propagation to a lesser degree (SMHI_ecearth3, CNRM_ACM, FGOALS-s2, LLNL_CAM5ZMMicro, and MPI_ECHAM6). Finally, more than half of the models show stationary or even westward-propagating signals, and the anomalies are confined to a much smaller zonal extent than that observed, indicating that

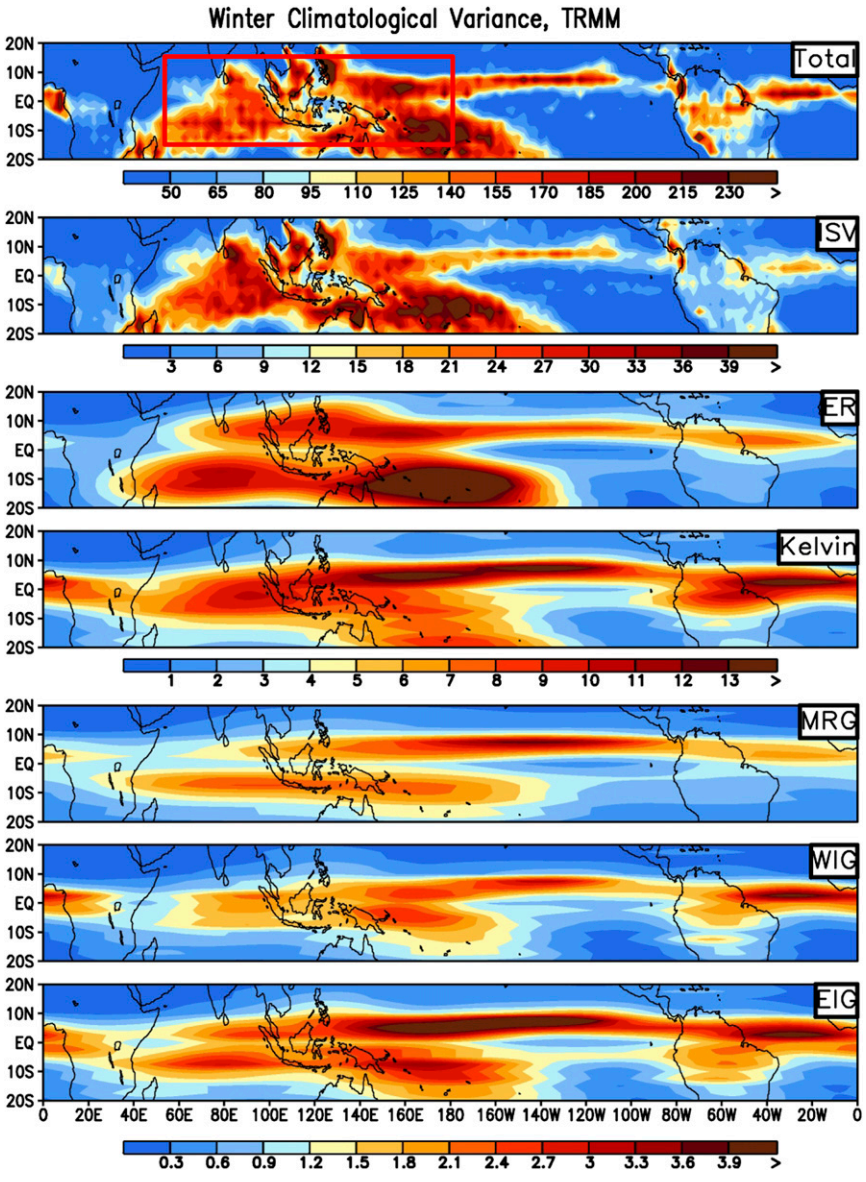


FIG. 1. Geographical distribution of boreal winter (December–April) mean variances of (top)–(bottom) the total, ISV, ER, Kelvin, MRG, WIG, and EIG wave modes based on the TRMM observations during 1998–2012 ($mm^2\,day^{-2}$). The red box encompasses from the Indian Ocean to the western Pacific Ocean region. (regional mean variances computed over this region are shown in Figs. 3b–e).

realistic simulation of the MJO is still a highly challenging issue. Nevertheless, compared to CMIP3 (Lin et al. 2006) and CMIP5 (Hung et al. 2013) ensembles, there are relatively more models that show reasonably good MJO simulation in the MJOTF/GASS project. One reason might be that some models have implemented specific strategies to help improve the model's MJO simulation, as that is the core target of this project. For example, SPCCSM implemented the "superparameterization" technique, which has been reported to lead to much improved MJO simulations (e.g., Benedict and Randall 2007). In TAMU_modCAM4, the "observed" vertical latent heating profile based on TRMM estimates was assimilated in order to accurately depict both the horizontal and vertical distributions of heating throughout the tropics, which was shown to help improve the MJO simulation significantly (Lappen and Schumacher 2012). More detailed discussions regarding the configurations of the participating models can be found in Jiang et al. (2015).

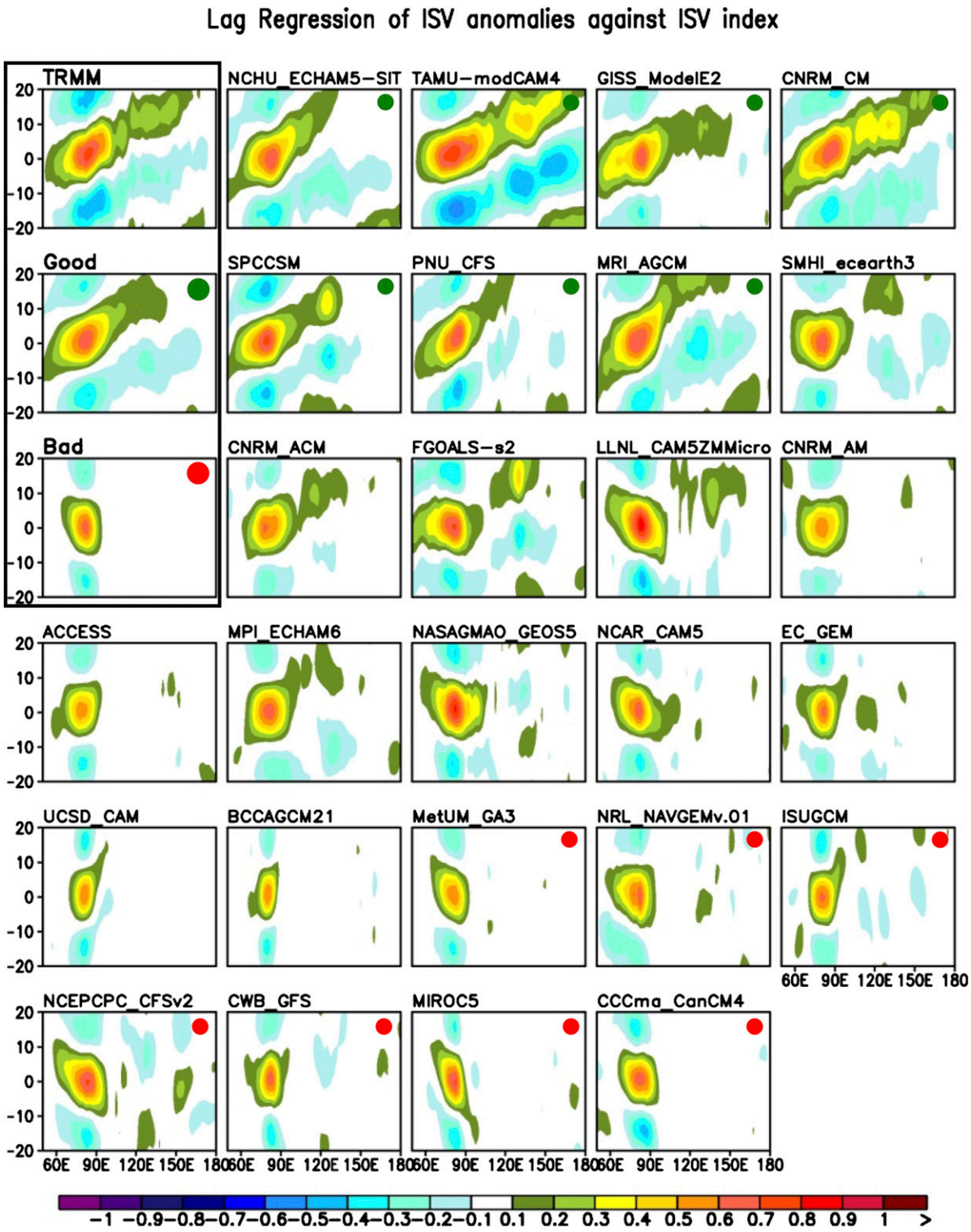


FIG. 2. Lag–longitude diagram of 10°S–10°N-averaged ISV (20–100-day filtered) precipitation anomalies (mm day$^{-1}$) regressed against the Indian Ocean ISV index, which is defined as the 20–100-day filtered precipitation anomalies averaged over 5°S–5°N, 75°E-85°E, at a lag time from day −20 to day 20; values correspond to 1 mm day$^{-1}$ ISV precipitation anomaly Pattern correlation between the panel for each model and that for TRMM observations is used to determine the MJO score for this model (see Fig. 3a) when combined with the western Pacific case. Except for TRMM, good composite, and bad composite panels outlined by a rectangle in the top left, the individual models are shown in descending order of their MJO scores moving down the figure from left to right. The good MJO composite (indicated by a large green dot) is based on the average of the seven best MJO models (indicated by a small green dot in top right of the panels), while the bad composite (indicated by a large red dot) is the average of the seven worst MJO models (indicated by a small red dot in top right of the panels).

The pattern correlation between the Hovmöller diagram computed from each model simulation and that based on the TRMM observations is then calculated over the domain of 50°E–180° and from day −20 to day 20 to evaluate how well the eastward-propagation pattern in that model resembles the observations. Then, the same procedure is applied to calculate another set of spatial correlation coefficients except that a reference box in the western Pacific (5°S–5°N, 130°–150°E) is used when conducting lag-regression analyses. The resulting patterns are very similar to those for the Indian Ocean case for all the models. The Pacific patterns are not shown here, but can be found in Fig. 4 of Jiang et al. (2015). Combining the coefficients based on both the Indian Ocean and the western Pacific cases, an MJO score can be finally assigned to each model simulation, which is shown in Table 3.

Results from the seven models (about one-quarter of total number of models) with the highest MJO scores are then composited to form the ''good'' MJO composite, and those from the seven models with the lowest MJO scores form the ''bad'' MJO composite. From Table 3, it can be seen that good MJO models have MJO scores larger than 0.85, while bad models have scores smaller than 0.65. The good composite again shows an eastward propagation close to the observations, while the bad composite displays a slight westward-propagation signal with a much smaller horizontal scale than is exhibited by the observed MJO (Fig. 2).

TABLE 3. MJO scores for 26 GCM simulations and TRMM observations, which are computed following the approach introduced in section 2d. The seven models (about one-quarter of the total number of models) with highest MJO scores (boldface) are used for the good MJO composite, while the seven models with lowest scores (italics) are used for the bad MJO composite.

| Model ID | MJO score |
|---|---|
| TRMM | *1.00* |
| NCHU_ECHAM5-SIT | *0.92* |
| TAMU-modCAM4 | *0.92* |
| GISS_ModelE2 | *0.91* |
| CNRM_CM | *0.90* |
| SPCCSM | *0.89* |
| MRI_AGCM | *0.89* |
| PNU_CFS | *0.87* |
| SMHI_ecearth3 | 0.83 |
| CNRM_ACM | 0.81 |
| FGOALS-s2 | 0.81 |
| LLNL_CAM5ZMMicro | 0.80 |
| CNRM_AM | 0.77 |
| ACCESS | 0.75 |
| MPI_ECHAM6 | 0.74 |
| NASAGMAO_GEOS5 | 0.73 |
| NCAR_CAM5 | 0.72 |
| EC_GEM | 0.71 |
| UCSD_CAM | 0.68 |
| BCCAGCM21 | 0.67 |
| MetUM_GA3 | **0.64** |
| NRL_NAVGEMv.01 | **0.64** |
| ISUGCM | **0.61** |
| MIROC5 | **0.59** |
| CWB_GFS | **0.59** |
| NCEPCPC_CFSv2 | **0.59** |
| CCCma_CanCM4 | **0.59** |

## 3. Climatology of ISV and CCEW activity

Before we proceed to explore the multiscale structure of the MJO, the climatology of the ISV and the CCEW activity is first examined in this section. The precipitation variances are first computed for the ISV and CCEWs, as well as the total wave mode over the entire tropics. Note that only winter seasons are used. The variances based on the TRMM observations have been shown in Fig. 1. For brevity, the counterparts of the 26 GCM simulations based on 20 winters (1991–2010) are not shown.

A regional mean of the wave variance is further obtained by averaging the variances at all grid points over the Indo-Pacific warm pool region (15°S–15°N, 50°E–180°; see the red box in the top panel of Fig. 1), which is the region with MJO activity. Note that there is also strong CCEW activity outside of the Indo–western Pacific region such as over South America and the tropical Atlantic Ocean. We chose to average the CCEW activity over the MJO-active region instead of the entire tropics as our focus is on the interaction between the CCEWs and the MJO. Nevertheless, we have performed exactly the same calculations except averaging over the entire tropics (15°S–15°N, all longitudes), and the results lead to the same conclusion.

### a. Strength of ISV and CCEW activity

The precipitation variances averaged over the Indo-Pacific warm pool region for each wave based on the 26 GCM simulations and TRMM observations are shown in Fig. 3. Examination of the climatology of the ISV and CCEW activity reveals a few interesting features.

First, the climatological wave activity exhibits large model-to-model variations: for example, for the ISV (Fig. 3b), the model with the largest variance (from BCCAGCM21) has variance that is about 4 times that of the smallest one (from LLNL_CAM5ZMMicro). Such large model-to-model variations in the amplitude of the wave variance are present in all wave modes, and can be traced back to the variation in the total wave variance (Fig. 3a). Note that the correlations between the ISV and different wave variances (bars in Figs. 3b–g) and the total variance (bars in Fig. 3a) among the 26 models and the TRMM data are all above 0.9. This indicates that a model with large (small) total precipitation variance

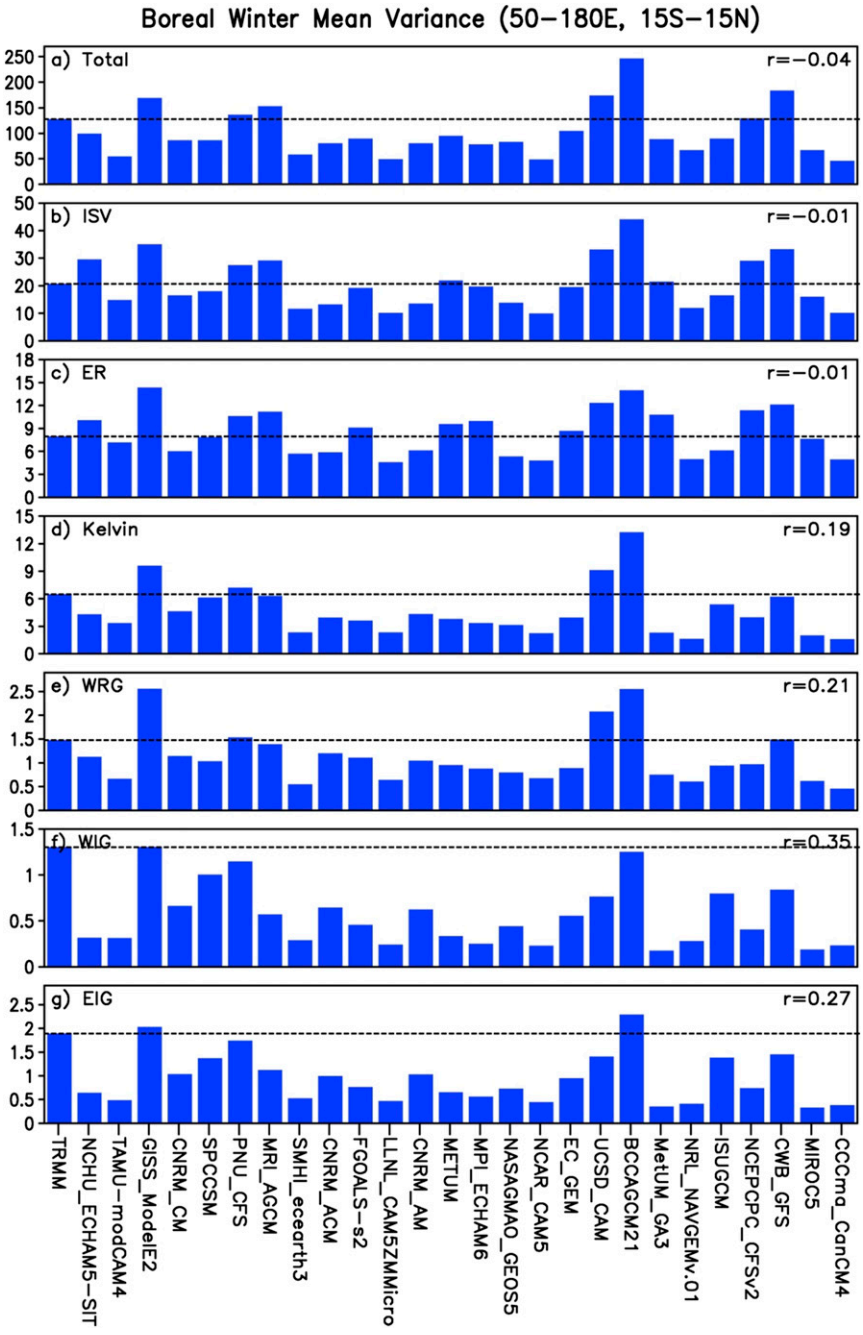


FIG. 3. Boreal winter (December–April) mean variances averaged over 15°S–15°N, 50°E–180° (indicated by the red box in Fig. 1) for 26 GCM models and TRMM observations for (a) total, (b) ISV, (c) ER, (d) Kelvin, (e) WRG, and (f) WIG and (g) EIG wave modes ($mm^2\ day^{-2}$). The period of model simulations is from 1991 to 2010, while for TRMM it is from 1998 to 2012. Dashed lines indicate the TRMM value of each mode. Value in the top-right corner of each panel indicates the correlation coefficient between the mean variance of each mode and the MJO score across 26 GCM models and TRMM observations.

tends to also exhibit strong (weak) precipitation variability associated with the ISV and CCEW modes.

Second, comparison between model simulations and the TRMM observations (denoted by the leftmost point and horizontal dotted lines) suggests that a longstanding problem in GCM simulations of tropical convection still exists: most of the participating models produce smaller precipitation variances compared to the observations

for the ISV and all CCEW modes, a phenomenon we call ''weak wave variance'' bias in this study. Table 2 lists the number of models that have weaker variance than that based on TRMM. It can be seen that 14 out of 26 models produce variance that is weaker than that found in TRMM for the ER mode, and 16 out of 26 for the ISV mode. Even worse, more than 20 models display the weak variance bias for the Kelvin, MRG, WIG, and EIG modes. Thus, the weak wave variance bias tends to be more severe for higher-frequency modes than for lower-frequency modes (ISV and ER).

This weak wave variance bias has already been identified for the CMIP3 and CMIP5 models (Lin et al. 2006; Hung et al. 2013). Nevertheless, our results suggest that models may be exhibiting some improvements in this aspect: in CMIP3 almost all GCMs show such a bias for all CCEWs; in CMIP5 this bias is still present for all the wave modes (except for EIG) in almost all the models, but the wave variances have been generally increased compared to their CMIP3 counterparts. Our results indicate that for models participating in the MJOTF/GASS MJO model intercomparison project, some models produce larger CCEW variances that those observed.

### b. *Linkage between the strength of the ISV and CCEW variance and the MJO score*

As discussed in section 3a, some models display better simulations of the strength of CCEWs than others. Given the fact that the MJO is often characterized as a slowly eastward-propagating, planetary-scale envelope of embedded CCEWs, one might hypothesize that a model's ability in realistically simulating the MJO may impact its ability to adequately simulate the strength of the CCEWs, or vice versa. To test this hypothesis, we will examine the possible linkage between the strength of each CCEW and the model's MJO performance across GCM simulations.

The correlation between the climatological variance of each wave mode (Figs. 3a–g) and the MJO score (Table 3) across 26 GCM simulations and TRMM observation is calculated and denoted by the number at the top-right corner of each panel in Fig. 3. It can be seen that there indeed exists some degree of positive correlation between the climatological wave strength and the MJO performance for the Kelvin, MRG, WIG, and EIG wave modes. The correlation coefficients range from 0.19 to 0.35 for 27 samples (26 models + TRMM), which, except for the WIG mode, are not significant at the 90% level based on a two-tailed Student's $t$ test. Furthermore, it is noted that the strengths of the ISV and ER, as well as the total wave activity, display nearly zero correlation with the MJO score.

It turns out that much stronger correlations between a model's MJO performance and its simulation of Kelvin, MRG, WIG, and EIG wave activity are revealed when the absolute wave variances are replaced by the ''fractional variances.'' Here, fractional variance is defined as the fraction of a wave mode's absolute variance relative to the total wave variance. The relations between the fractional variance of the ISV and CCEWs and the MJO score in the 26 GCM simulations plus the TRMM observation are displayed by scatterplots in Fig. 4. Strong correlations between the MJO score and the fractional variances are found for the Kelvin, MRG, WIG, and EIG wave modes, with correlation coefficients of 0.58, 0.58, 0.51, and 0.49, respectively, all significant at the 99% confidence level based on a two-tailed Student's $t$ test. These statistically significant correlations indicate that models having better MJO performance tend to simulate larger Kelvin, MRG, WIG, and EIG fractional variances, and vice versa (Figs. 4b–e). Recall the weak wave variance bias that existed in GCM simulations of the CCEWs discussed above, which is especially severe for high-frequency modes such as Kelvin, MRG, WIG, and EIG waves (Table 2). Thus, larger fractional variances of these modes mean that the weak variance bias is less severe in these models (Figs. 4b–e), which is likely also related to the improvement of the model's MJO simulation. This suggests that when a model has a better MJO, its total variance is also more coherently organized into CCEW modes.

Another important CCEW is the ER wave. Figures 4f and 3c suggest that the strength of the ER mode has no correlation with the model's MJO performance in terms of either fractional or absolute variance. Note that compared to Kelvin, MRG, WIG, and EIG waves, the ER wave is a relatively larger-scale and lower-frequency mode.

It should also be noted that the strength of the ISV itself exhibits very weak correlation with the model's MJO performance when the fractional variance is used (0.08; see Fig. 4a). The correlation decreases to about zero (−0.01) when the absolute variance is considered (Fig. 3c). This is different from what is shown by Kim et al. (2011), in which a significant positive correlation is found between the ISV variance and the MJO performance. Note that in their study, the MJO performance is quantified by the ratio of the MJO (wavenumbers 1–3 and 30–60 day) variance to its westward counterpart, which highly correlates with our MJO score (0.77; Jiang et al. (2015)) as both methods concern the eastward-propagating feature of the ISV band. The discrepancy between our results and those of Kim et al. (2011) in terms of very weak or strong positive correlation between the ISV variance strength and the MJO performance might be partly due to the fact that their results are based on a rather limited number of climate models: they examined 10 simulations from five AGCMs (some have

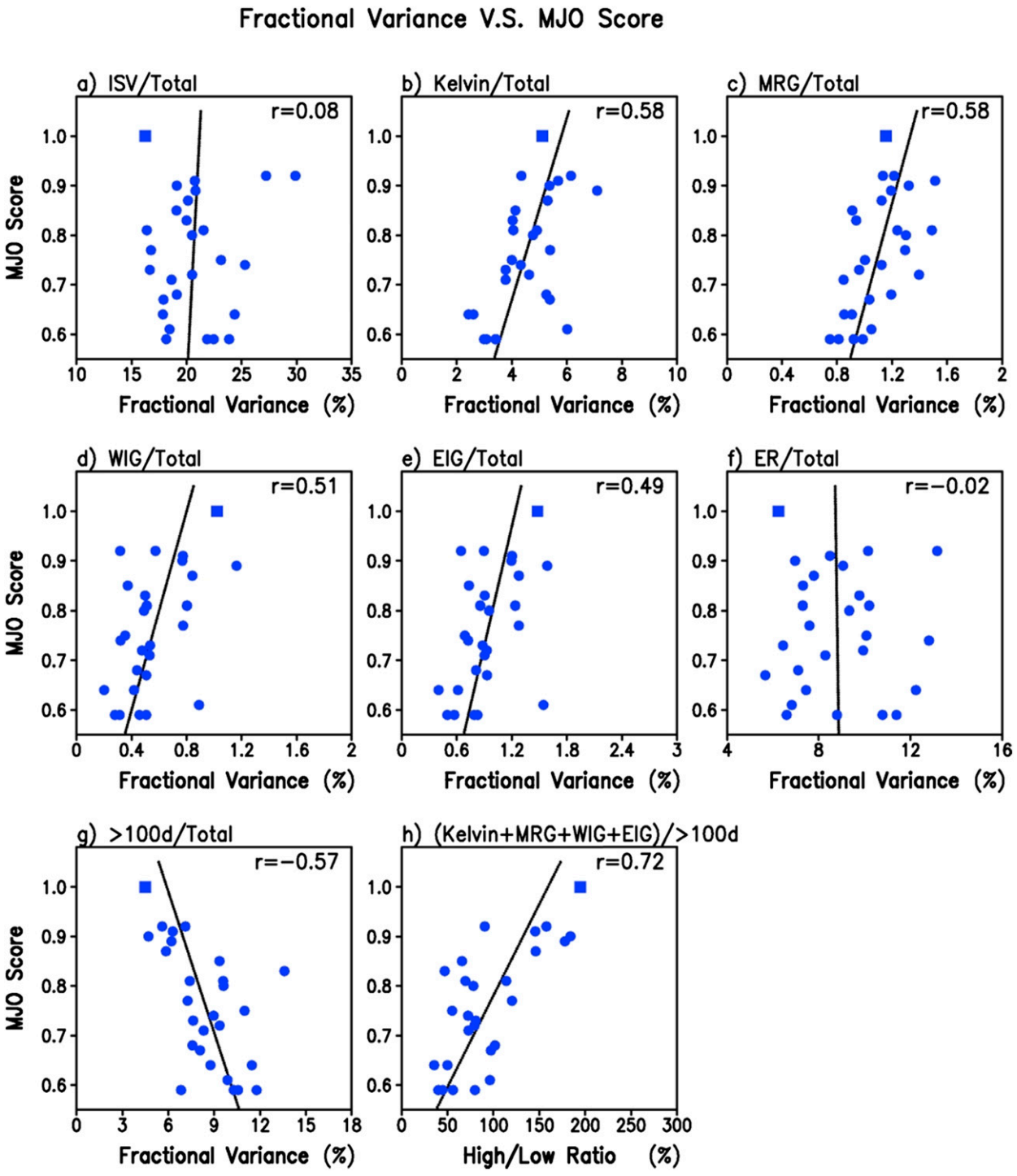


FIG. 4. Scatterplots of the MJO score and the fractions of (a) ISV, (b) Kelvin, (c) MRG, (d) WIG, (e) EIG, (f) ER, and (g) low-frequency (period > 100 day) mode variance relative to the total variance, and (h) the summed Kelvin, MRG, and WIG and EIG variances relative to the low-frequency mode variance. Filled circles represent individual GCM simulations, while a filled square represents the TRMM observations. The correlation coefficient of each scatterplot is indicated by the number in the top-right corner of the panel. Correlation coefficients that are statistically significant at the 90%, 95%, and 99% confidence levels for 27 samples are 0.32, 0.37, and 0.48 respectively, based on the two-tailed Student's *t* test.

sensitivity experiments by tuning cumulus parameterization), and furthermore, two of the five models are different versions of the Community Atmosphere Model (CAM). In this sense, our conclusion is probably more robust than theirs.

As we have shown above, strong linkage between a model's MJO and CCEW performance can only be found for the Kelvin, MRG, WIG, and EIG wave modes, with such a linkage being absent for the ER mode and the ISV. Since the Kelvin, MRG, WIG, and EIG waves are all located over the high-frequency end of the precipitation spectrum, it is of interest to examine the behavior of the precipitation anomalies toward the other end of the spectrum. Here, we examine the low-frequency part of the precipitation, defined as precipitation anomalies with periods longer than 100 days, which we denote as the >100 day component. The correlation between its fractional variance and the MJO score is shown in Fig. 4g, which is highly negative (−0.57), indicating that the better a model performs in simulating the MJO, the smaller is the fractional variance of its low-frequency band. This is opposite to the Kelvin, MRG, WIG, and EIG cases. Combining the high- and low-frequency components together, it is suggested that a model with better MJO performance tends to have relatively stronger variance in high-frequency modes and weaker variance in the low-frequency mode, which is further clearly revealed in Fig. 4h where a scatterplot of the ratio of the high-frequency band to the low-frequency band and the MJO score is shown (the correlation is as high as 0.72). It should also be noted that in all cases in Fig. 4, except for the ISV and ER modes, models having higher MJO scores tend to have fractional variance ratios that are closer to those observed.

This finding is encouraging in the sense that the increase in high-frequency precipitation variance and the reduction in low-frequency precipitation variance correspond to the alleviation of long-existing problems in GCM simulations. Previous studies based on CMIP3 and CMIP5 models (Lin et al. 2006; Hung et al. 2013) have found that the simulated precipitation tends to contain too much variance at the low-frequency end of the space–time spectrum, which was referred to as the overreddened spectrum phenomenon. This phenomenon was also noticed as a tendency for too much persistent light rain in other studies (Dai 2006; Boberg et al. 2009). Along with the overestimation of the low-frequency precipitation variance, Lin et al. (2006) and Hung et al. (2013) also found that the precipitation variance at the high-frequency end is significantly underestimated, such that the CCEW variance is much weaker than that observed. Thus, the tendency for increased high-frequency precipitation variance and decreased low-frequency precipitation variance occurs in conjunction with models having better MJO scores corresponds to an alleviation of the aforementioned model deficiencies in simulations using these models.

Furthermore, the composite results based on the top seven good and bottom seven bad MJO models according to their MJO scores are summarized in Fig. 5. Again, it can be seen that the fractional variances of Kelvin, MRG, WIG, and EIG wave modes in the good models are systematically larger than their counterparts in the bad models, and closer to the observational results. The magnitudes of these high-frequency mode variances in the good model composites are about 1.5 times of those in the bad model composites. At the same time, the fractional variance of the low-frequency variability is much smaller in the good model composite than that in the bad composite and, thus, more consistent with the observational result. It is also noted that the composite ER and ISV wave variances in both groups have almost the same magnitude and are both larger than those observed. Note that ER wave forms essential part of the ISV mode, thus strongly contributing to the stronger-than-TRMM ISV variance.

## 4. Implication of the multiscale interaction between CCEW and MJO for the MJO performance

In the preceding section, we have revealed a strong linkage between the climatological behavior of the high-frequency CCEW (Kelvin, MRG, WIG, and EIG waves) activity and the MJO performance in the climate models. Here, we will further examine the multiscale interaction between the CCEW activity and the MJO in these models to see if there is any systematic relationship between the representation of the CCEW–MJO interaction and the simulation of the MJO.

The linear regression analysis is used here to explore the multiscale interaction between the CCEWs and the MJO. To be specific, the time series of the squared CCEW anomalies during the entire period at each grid point over the Indo–western Pacific are regressed onto the Indian Ocean ISV index (20–100-day filtered precipitation anomalies averaged over 5°S–5°N and 75°–85°E). The regression coefficient $\beta$ at each point can then be computed using Eq. (1). Here, $s_x$ is the standard deviation of the ISV index, $s_y$ is the standard deviation of the time series of the squared CCEW anomalies, and $r_{xy}$ is the correlation between them. Thus, the regression coefficient represents the conditionally composited CCEW variance, and we call it regressed CCEW variance or ISV-associated CCEW variance in later discussions for brevity. Note that the strength of the ISV precipitation varies in different GCM simulations (Fig. 3c); thus, the standard

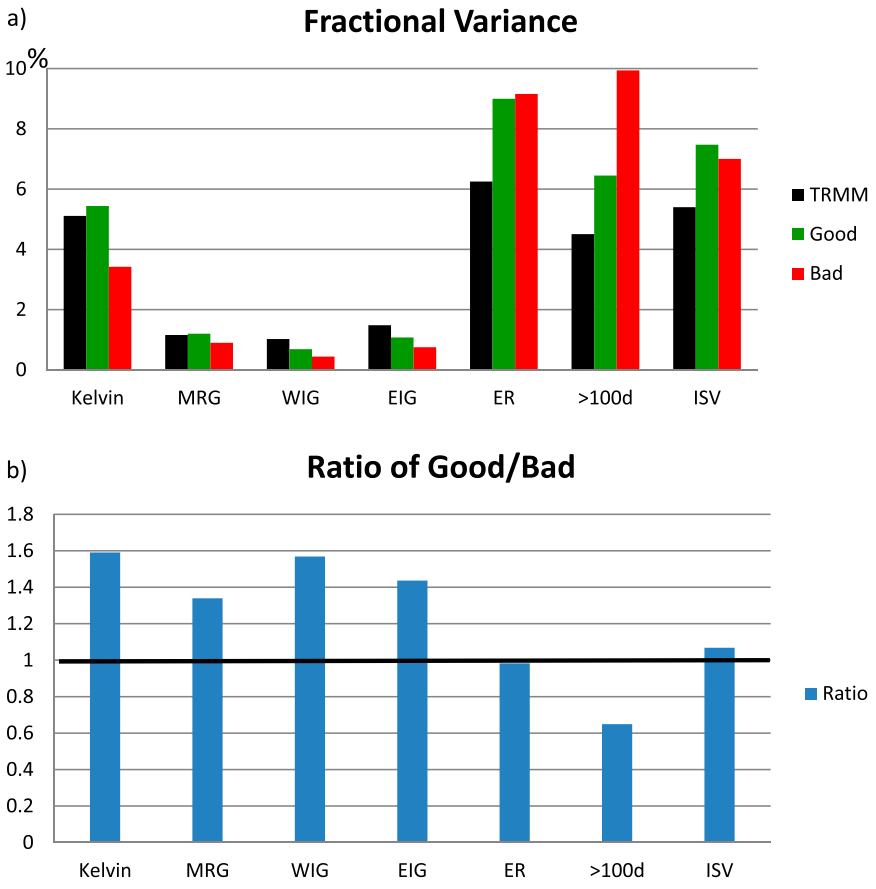


FIG. 5. (a) Fractional variances of the ISV and CCEW modes composited for the seven good and bad MJO models, as well as for TRMM observations. Values shown for the ISV are one-third of their original total in order to be accommodated to the same scale. (b) Ratios of the fractional variances between the good model composite and bad model composite for the ISV and CCEW modes.

deviation of the ISV index is different for different models. Nevertheless, the regressed CCEW variance determined by Eq. (1) represents the expected value of the CCEW variance corresponding to one unit of ISV precipitation anomaly (1 mm day$^{-1}$ here). Thus, the model-to-model difference in the amplitude of the ISV index has been eliminated, and direct comparison among the models can be made.

Figure 6 shows the spatial distribution of the regressed Kelvin wave variance (shading) together with the correlation coefficients between the Kelvin variance and the ISV index (light gray contours). The MJO envelope is also outlined by the thick black contours, which corresponds to $\pm 0.2$ mm day$^{-1}$ of the regressed ISV anomalies in Fig. 2. Results are shown for the TRMM observations, composites of good and bad MJO models, as well as individual models, which are displayed in descending order based on their MJO scores. Examining the TRMM observations, it can be seen that the regressed Kelvin wave activity is generally positive within the positive ISV convection envelope, and negative for the negative envelope, which is consistent with the findings of previous studies that the Kelvin wave activity is enhanced in association with the convectively active MJO anomalies, and reduced when the MJO convection is suppressed (Roundy 2008; Guo et al. 2014). In addition to the overall collocation to the ISV envelope, the enhancement of the Kelvin wave activity is also noticed to extend slightly farther to the west of the ISV envelope than to the east side. However, this westward extension appears to be basin dependent. For example, the regression of the Kelvin wave activity against a western Pacific ISV index (5°S–5°N, 145°–155°E) shows no preferred extension on either side of the ISV envelope, with its enhancement (reduction) primarily in phase with the active (suppressed) ISV envelope (not shown).

The observed features are well represented in the composite based on the good MJO models, but poorly simulated in the bad MJO models, as basically very weak regressed Kelvin variance is found in these models. Keep in mind that the results have already been normalized for

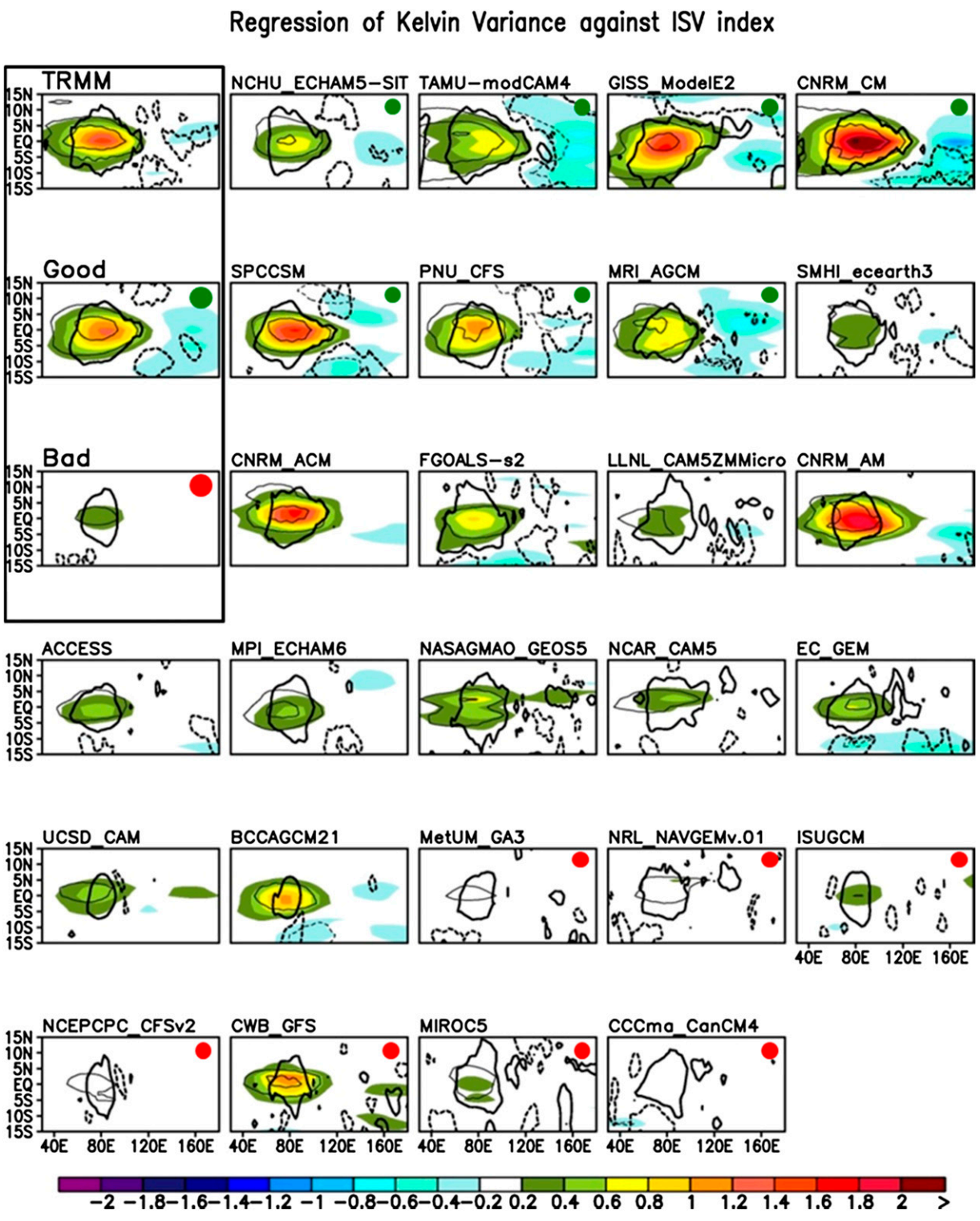


FIG. 6. Latitude–longitude pattern of the Kelvin wave variance (shading; mm day$^{-1}$) regressed against the Indian Ocean ISV index, which is defined as the 20–100-day filtered precipitation anomalies averaged over 5°S–5°N, 75°–85°E; the values of the Kelvin variance correspond to 1 ISV precipitation anomaly. Light gray contours are the correlation coefficients between the Kelvin wave variance and the ISV index. The contour interval is 0.1, and the contour of 0 is omitted. Thick black contours outline the ±0.2 mm day$^{-1}$ lines of the regressed ISV anomalies themselves to represent the MJO envelope. The good MJO composite (indicated by a large green dot) comes from the average of the seven best MJO models (indicated by a small green dot in the top right of the panels), while the bad composite (indicated by a large red dot) is from the seven worst MJO models (indicated by a small red dot in the top right of the panels).

overall ISV strength and thus this indicates that for bad MJO models there simply is not a connection between the MJO and local Kelvin wave variance. Put another way, this means there is less coherence between Kelvin wave activity and the ISV in bad models compared to the good models and to the observations, regardless of the overall ISV amplitude. Figure 6 also illustrates that the magnitude of the ISV-associated Kelvin variance differs greatly from model to model, with a tendency for good MJO models to exhibit stronger Kelvin variance than the bad MJO models for a given amount of ISV precipitation anomaly. This result is clearly illustrated by the contrast between the good and bad composites.

In addition to the concurrent regression maps, the temporal evolution of the Kelvin wave activity with respect to the ISV variation is further examined using the lag regression analysis (Fig. 7). The time series of the squared Kelvin anomalies are first averaged between 10°S and 10°N and, then, regressed against the ISV index with a lag from −20 to 20 days. The Hovmöller diagram shows that in the observations and the good MJO models, the ISV anomalies are manifested as a large-scale, eastward-propagating intraseasonal wave mode, which is the typical MJO event. In these models, the Kelvin wave activity is found to be strongly enhanced (suppressed) associated with the positive (negative) ISV convection complex, and propagates eastward along with the eastward propagation of the ISV convection. For the bad MJO models, the ISV anomalies are either quasi-stationary or even westward propagating. Furthermore, they are confined within a horizontal scale much smaller than that found in the good models and observations. This suggests that the ISV anomalies in the bad models do not successfully manifest a coherent Kelvin wave–MJO relationship. For these models, the regressed Kelvin wave variances are generally very weak; the correlations between the Kelvin wave variance and the ISV index are small, which suggests little coherence is found between the Kelvin waves and the ISV anomalies in these models in contrast to the situation found for the good MJO models.

The above results found for the Kelvin wave mode also generally hold true for the MRG, WIG, and EIG wave modes (see Fig. 8), but quite different results are obtained for the ER wave mode. Figure 9 shows that the magnitudes of the regressed ER wave variances between the good and bad MJO models do not exhibit the kind of systematic difference found in the Kelvin, MRG, WIG, and EIG cases. Nevertheless, there are hints that the good MJO models simulate the spatial–temporal evolution of the ER variance generally better than that simulated by the bad models (cf. the good and bad composites to the TRMM Hovmöller plot in Fig. 9).

Figures 6 and 7 together suggest that the better a model simulates the MJO, the stronger the Kelvin wave variance with respect to one unit of ISV anomaly it tends to generate. This relationship is further quantified by the scatterplot shown in Fig. 10a, in which the ISV-associated Kelvin wave variances are averaged over a box covering 5°S–5°N, 75°–85°E, which is also the area used to compute the ISV index, based on the concurrent regression map (Fig. 6). A positive correlation coefficient of 0.61 is found between the ISV-associated Kelvin wave variance and the MJO score across multiple models and observations (Fig. 10a), which is statistically significant at the 99% confidence level. Large positive correlations are also found for the MRG, WIG, and EIG wave modes (Figs. 10b–d), which further shows the similarity among these synoptic waves in terms of the interactions between them and the ISV mode. On the other hand, a statistically insignificant negative correlation is found for the ER wave mode (Fig. 11e).

Figure 11a shows that the models with good simulations of the MJO have larger Kelvin, MRG, WIG, and EIG wave variances for the same unit variation of ISV precipitation, and have values that are more consistent with the observations. For these four wave modes, good MJO models have on average 2.5–4 times the ISV-related variances found in bad MJO models (Fig. 11b). Taken together, results shown in Figs. 6–11 suggest that there is stronger coherence and interaction between the ISV and these synoptic wave modes in the good MJO models.

Note that despite the importance of the multiscale interaction in simulating a realistic MJO as suggested above, our current study does not provide a physical explanation for how this mechanism might work. Previous studies (Majda and Biello 2004; Biello and Majda 2005; Majda and Stechmann 2009; Wang and Liu 2011; Liu and Wang 2012; Sobel and Maloney 2013) have examined the roles of multiscale interaction in the existence and propagation of the MJO using theoretical models. Nevertheless, the models used in these studies are very simple, and the results often rely on important assumptions, which might not be consistent with the observations. Therefore, continued efforts are still needed to advance our understanding of the roles of the multiscale interactions in the MJO dynamics. Our results based on examination of a large number of comprehensive GCM simulations add useful information to these simplified/idealized theoretical studies.

## 5. Conclusions and discussion

The MJO and CCEWs, including the Kelvin, ER, MRG, EIG, and WIG wave modes, account for the major portion of the organized subseasonal variability of

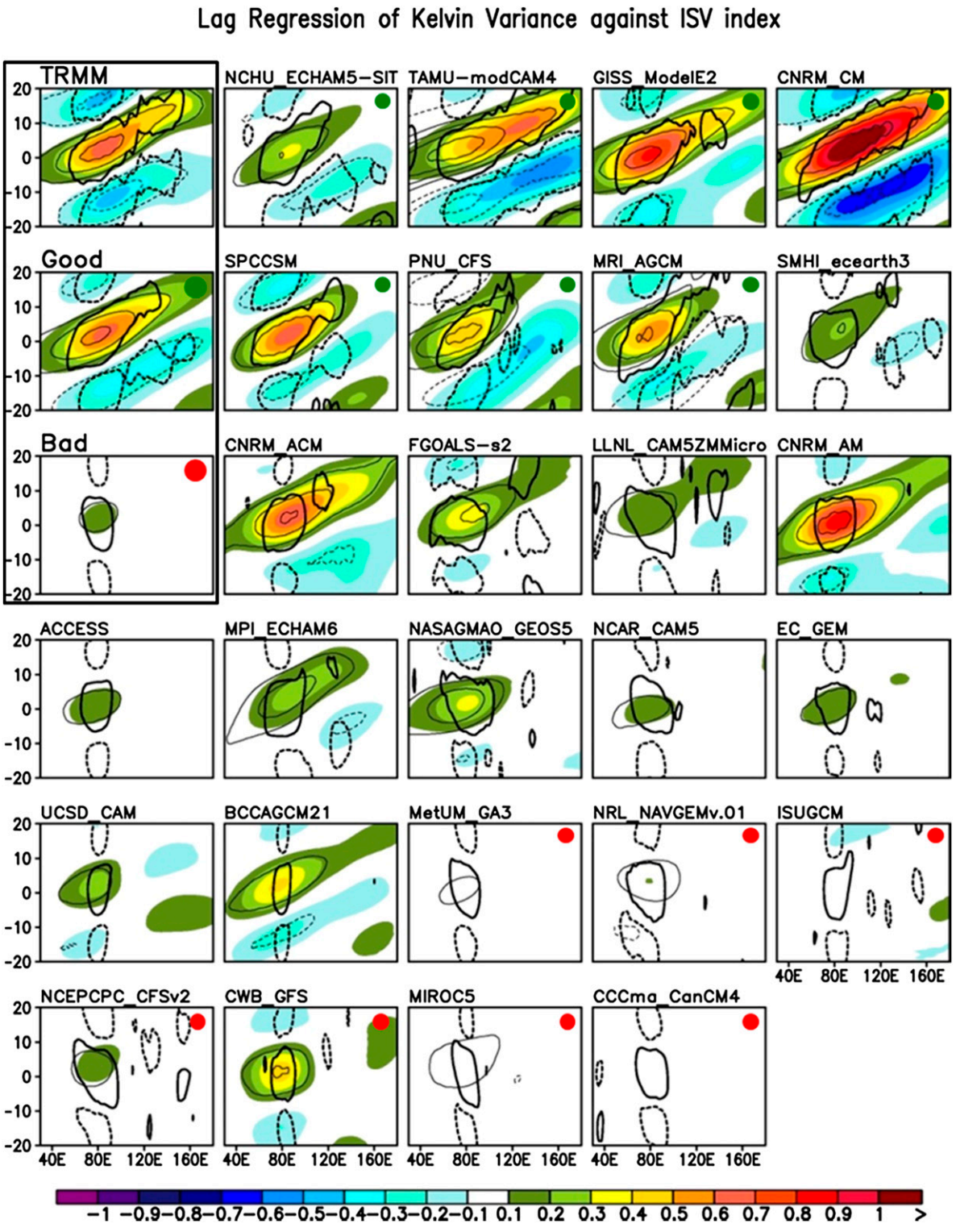


FIG. 7. Lag–longitude diagram of 10°S–10°N-averaged Kelvin variance (shading; $mm^2\ day^{-2}$) regressed against the Indian Ocean ISV index, which is defined as the 20–100-day filtered precipitation anomalies averaged over 5°S–5°N, 75°–85°E, at a lag time from day −20 to day 20; the values of the Kelvin variance correspond to 1 $mm\ day^{-1}$ ISV precipitation anomaly. Light gray contours are the correlation coefficients between the Kelvin wave variance and the ISV index. The contour interval is 0.1, and the contour of 0 is omitted. Thick black contours outline the $\pm 0.2\ mm\ day^{-1}$ lines of the regressed ISV anomalies themselves to represent the MJO envelope. The good MJO composite (indicated by a large green dot) comes from the average of the seven best MJO models (indicated by a small green dot in the top right of the panels), while the bad composite (indicated by a large red dot) is from the seven worst MJO models (indicated by a small red dot in the top right of the panels).

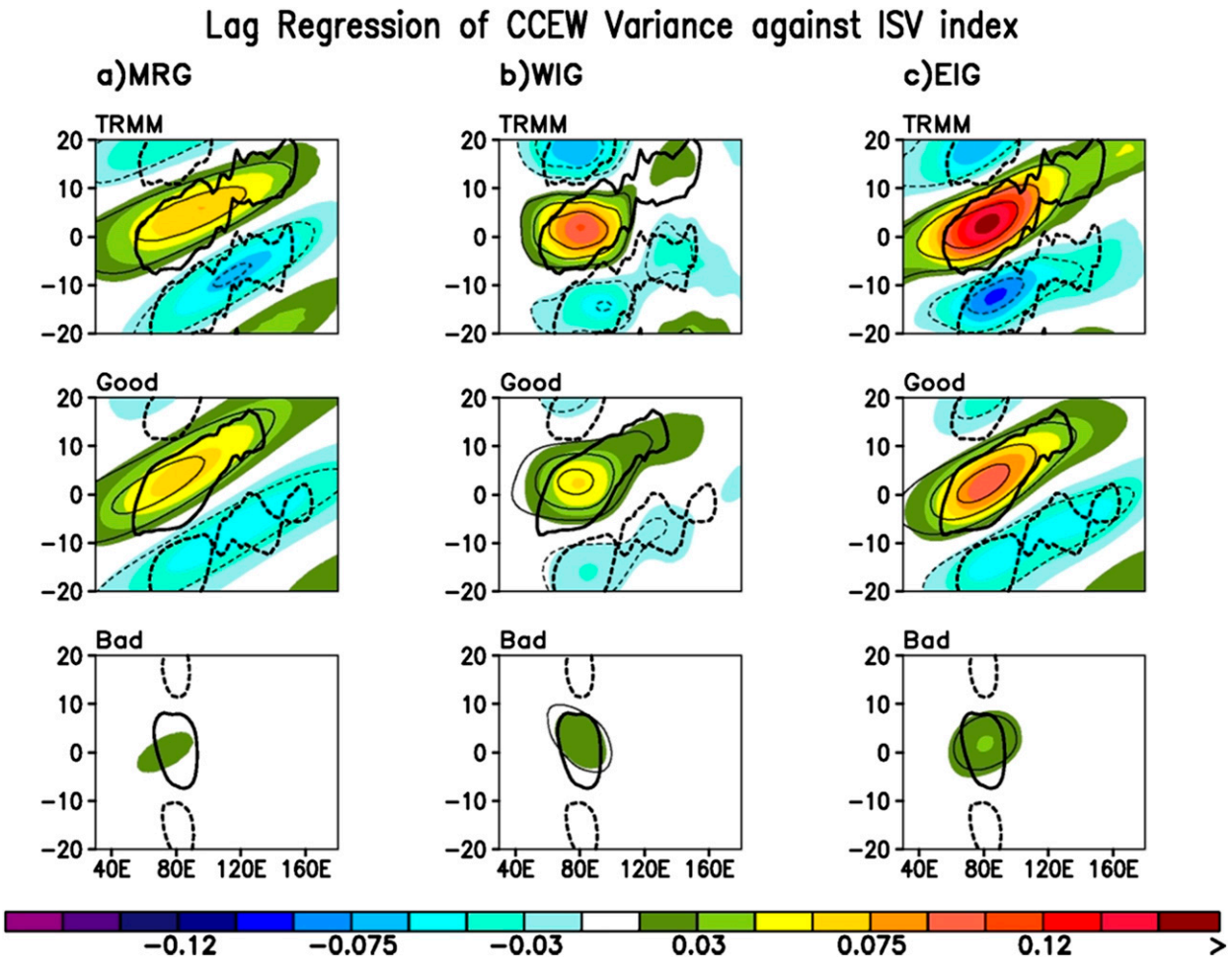


FIG. 8. As in Fig. 7, but for (a) MRG, (b) WIG, and (c) EIG wave modes, only the (top) TRMM observations and the (middle) good and (bottom) bad MJO model composites are shown.

the tropical convection. In this study, the activity of these wave modes has been examined using 20-yr precipitation output from 26 GCM models participating in the MJOTF/GASS joint model intercomparison project, and compared to the TRMM observations.

A model's performance in simulating the MJO has been evaluated based on how faithfully it reproduces the eastward propagation of the winter ISV mode compared to the TRMM observations following the approach of Jiang et al. (2015). It is found that about one-quarter of the models can capture a coherent eastward-propagating feature—reminiscent of the MJO—quite well, and a few more are able to simulate such a feature to a modest degree. Meanwhile, more than half of the models show stationary or even westward propagation with a much narrower than observed zonal scale (Jiang et al. 2015).

Relationships between a model's performance in simulating the MJO and the simulated CCEW activity across the 26 model simulations have been explored from two perspectives. First, strong positive correlations have been found between a model's MJO performance and the fractional wave variances of higher-frequency wave modes including Kelvin, MRG, WIG, and EIG (Figs. 4b–e), and strong negative correlation with the low-frequency variability component (>100 days) (Fig. 4g). Combining the high-frequency and low-frequency components together, it is found that a model with better MJO performance tends to have stronger variance in high-frequency modes and weaker variance in the low-frequency mode (Fig. 4h; the correlation is as high as 0.72). The usage of the fractional wave variance, as defined by the fraction of absolute variance of a certain wave mode relative to the total wave variance, is essential for revealing the above relationship. Positive but not statistically significant correlations are found in many previous multimodel comparison studies when the absolute wave variance was used. Results of the "good" and "bad" composites based on the seven models with the best or the

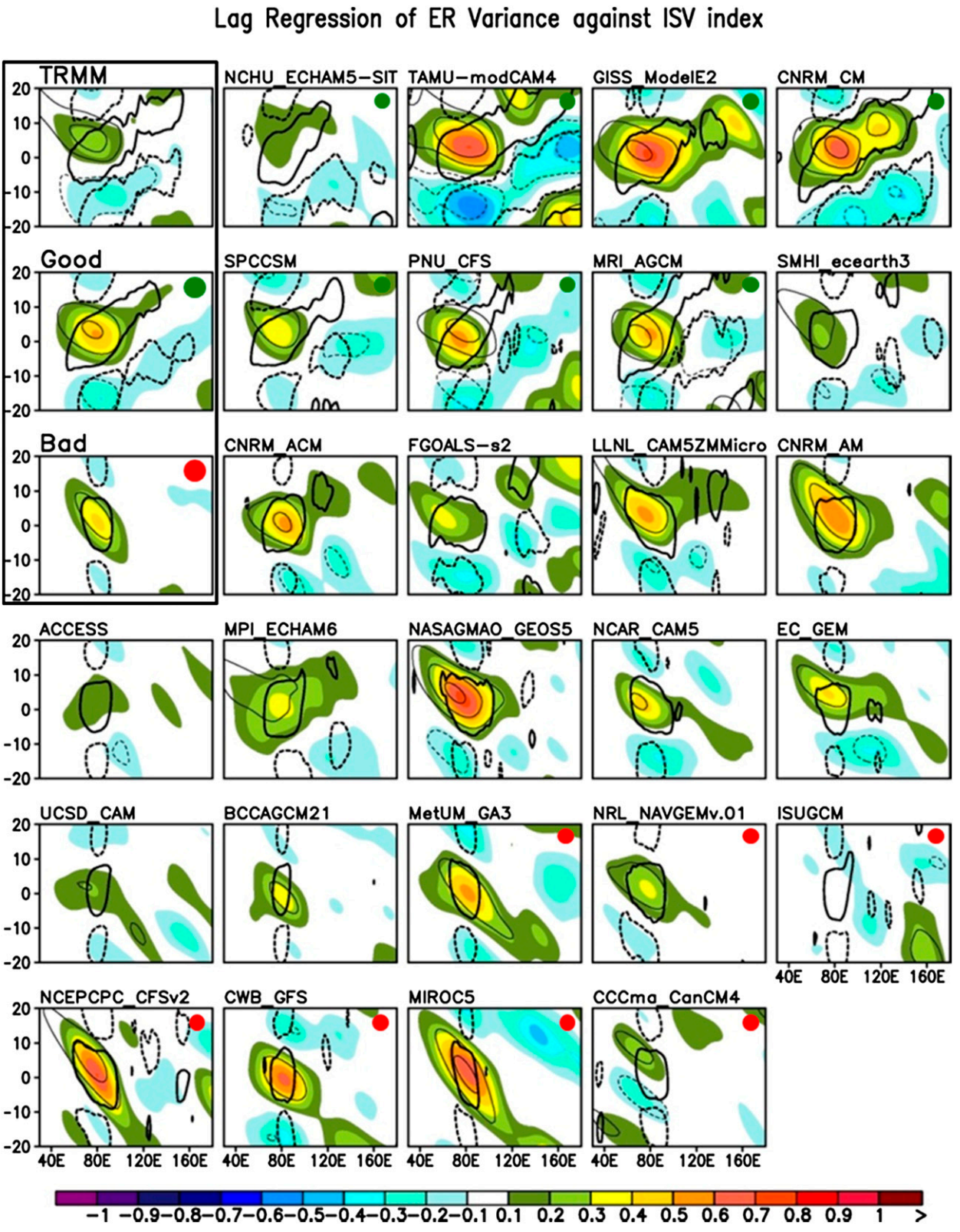


FIG. 9. As in Fig. 7, but for ER waves. The ER wave anomalies are averaged between 15°S and 15°N instead of between 10°S and 10°N, as is the case for the other waves.

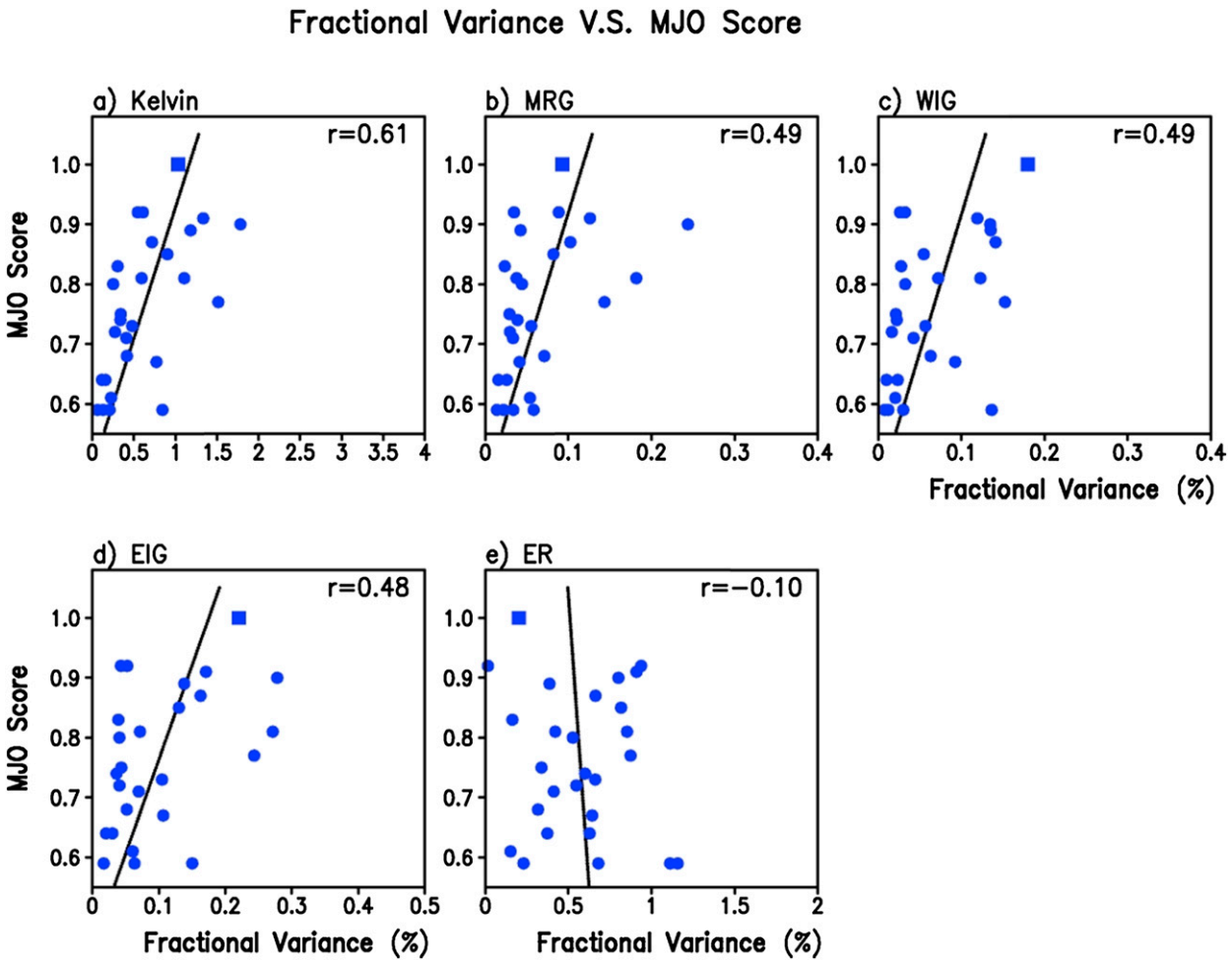


FIG. 10. Scatterplots of the MJO score and the ISV associated variances of (a) Kelvin, (b) MRG, (c) WIG, (d) EIG, and (f) ER wave modes. Here, the values of the ISV-associated CCEW variances are computed by averaging the CCEW variances in the concurrent regression maps over 5°S–5°N, 75°–85°E. For example, values of the Kelvin case come from the averages of the Kelvin variances in Fig. 6 over the averaging domain. Filled circles represent individual GCM simulations, while the filled square represents the TRMM observations. The correlation coefficient of each scatterplot is indicated by the number at the top-right corner of the panel. Correlation coefficients that are statistically significant at the 90%, 95%, and 99% confidence levels for 27 samples are 0.32, 0.37, or 0.48 respectively, based on the two-tailed Student's *t* test.

worst MJO performance further confirm that the magnitudes of the fractional variances of Kelvin, MRG, WIG, and EIG wave modes in the good composites are about 1.5 times of those in the bad composites, and have values closer to the observed results (Fig. 5).

A linear regression analysis further suggests that good MJO models tend to exhibit stronger Kelvin, MRG, WIG, and EIG variances than do the bad MJO models with respect to a similar amount of ISV precipitation anomaly. This tendency is associated with the spatial–temporal evolution of the ISV events themselves and, thus, is indicative of how these wave variances and MJO events are related. Strong positive correlations are found between the magnitudes of the ISV-associated wave variances for these waves and a model's MJO performance across the model ensemble (Figs. 10a–d). It is further shown that for these four wave modes, good MJO model composites have on average 2.5–4 times the ISV-related variances found in bad composites, and have ISV-related variances that are more consistent with the observations (Fig. 11). However, it should also be noted that little correlation has been found between the strength of the wave variance for the ISV mode itself as well as that for the ER mode and a model's MJO performance.

Figure 12 shows schematic plots that illustrate the main differences found between the good and bad MJO models. Compared to the bad MJO models, the high-frequency CCEWs (i.e., Kelvin, MRG, WIG, and EIG) are more realistically simulated, and this is illustrated as

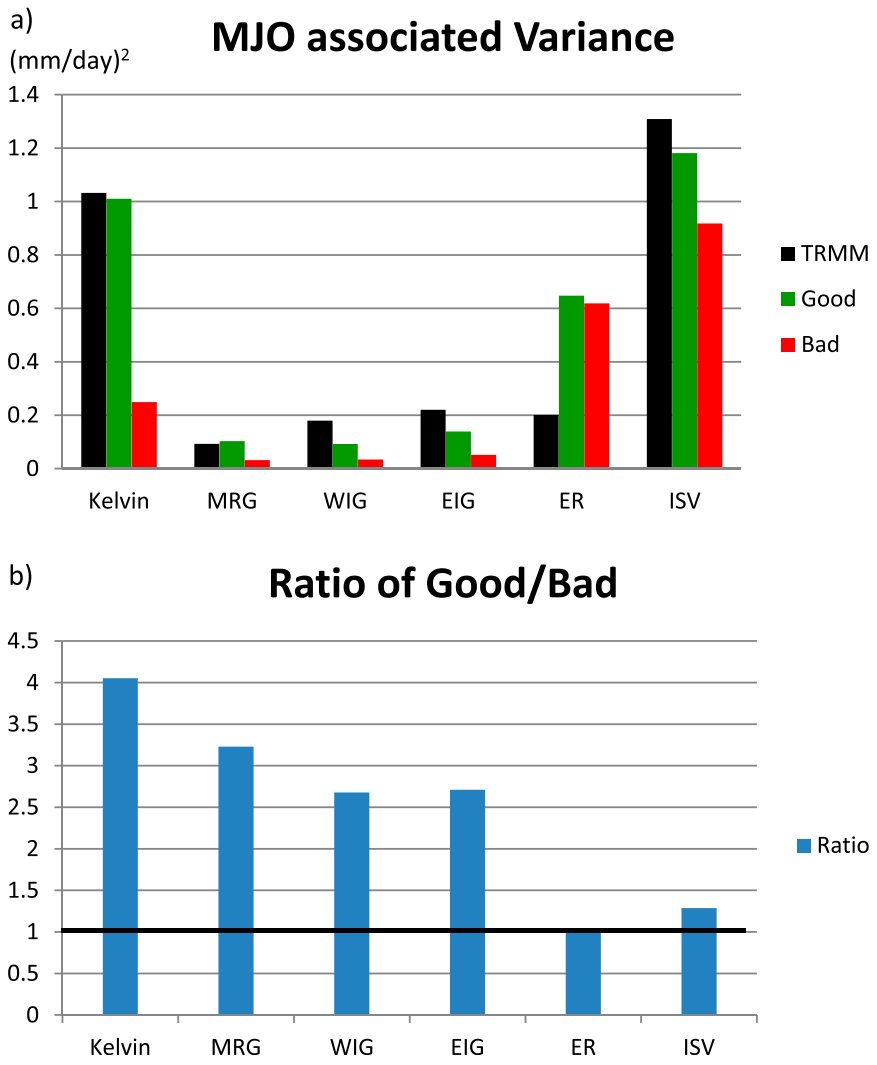


FIG. 11. (a) ISV-associated variances of the Kelvin, MRG, WIG, EIG, and ER wave modes composited for the seven good and bad MJO models, as well as TRMM observations. (b) Ratios of the composite variances between the good and bad model groups for these waves. As a reference, the composites of the standard deviations of the ISV index are also shown. Values shown for the ISV in (a) are one-third of their original values in order to be presented at the same scale.

a stronger climatological variance (in terms of fraction to the total anomalies) for these waves. In addition, the CCEWs in these models exhibit better coherence with the MJO, which is illustrated as enhanced CCEW activity within the active MJO convection envelope in contrast to reduced coincidence between the CCEW enhancement and the MJO envelope in Fig. 12b. Both features may contribute to the better MJO performance in these models. Note that although we denote the blue curve in the bad MJO models as an "MJO envelope," it is more likely a random intraseasonal oscillation than a real MJO mode; thus, we make it narrower and weaker compared to the blue envelope in the good MJO models (see the comparison between the good and bad cases in Fig. 2).

The finding that good MJO models tend to have stronger climatological wave variances (in terms of the fraction of the total variance), as well as ISV-associated wave variances for the high-frequency wave modes (Kelvin, MRG, WIG, and EIG), are hypothesized to be related to the following points. The former tendency for good MJO models corresponds to the alleviation of longstanding deficiencies in simulating tropical precipitation in climate models [i.e., too weak (strong) variance in the high-frequency (low frequency) spectrum of the precipitation relative to the frequency of the MJO].

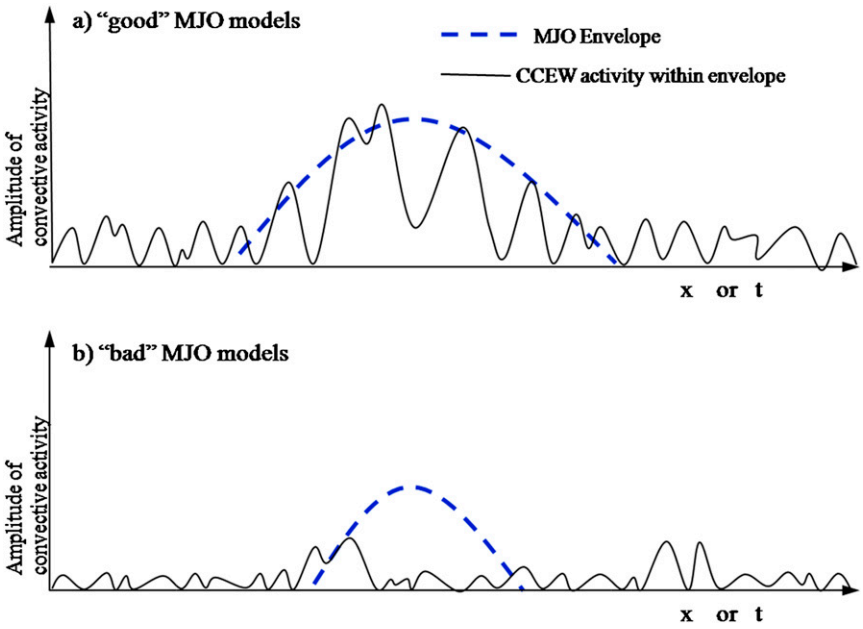


FIG. 12. Schematic illustration of the multiscale structure of the MJO and the embedded higher-frequency CCEWs (i.e., namely Kelvin, MRG, WIG, and EIG) simulated in the (a) good and (b) bad MJO models.

The latter tendency suggests better coherence and stronger interaction between the synoptic waves and the ISV envelope they form in, which has been thought to play a critical role in the existence and propagation of the MJO. It is likely that these two conditions have some bearing on the improved MJO performance that has been achieved in the good MJO models.

In addition, the self-similarity nature of organized convective systems (e.g., Majda 2007; Khouider and Majda 2008a,b; Kiladis et al. 2009) may be a possible factor giving rise to the result that a better MJO model would also have better representation of the CCEW variance: a good convective parameterization might better simulate the organized convection across multiple scales from the MJO through CCEWs to mesoscale convective systems, as well as the interactions among them. Nevertheless, we have found no clear relationship between MJO performance and the convective parameterizations used in these models, but such possible linkages could be masked by the modification of the details of the convective parameterization, such as using different triggering mechanisms, closure schemes, or nonlinear interactions between convection and other parameterizations (e.g., the boundary layer scheme or cloud microphysics). Future work is needed to improve our understanding on this perspective.

Our results support the systematic relationship between the MJO and the embedded CCEWs within the multiscale interaction framework. This was found by examining a large number of the state-of-the-art GCM simulations that integrate comprehensive physical processes, thus adding useful information to previous studies that mainly employed simplified theoretical models. However, the current study has not provided any in-depth diagnoses on the two-way interaction between the MJO and the CCEWs, such as how the MJO modulates the CCEWs through its influence on the large-scale environmental fields, or how the CCEWs feed back to the MJO through upscale transports of, for example, momentum, temperature, and moisture. These issues will be explored in future studies. Furthermore, although CMIP3 and CMIP5 model ensembles do not contain many models with realistic enough MJO simulations, there may still be enough good models to make it worthwhile to apply the analyses conducted in this study to see how well the aforementioned tendencies between the CCEW activity and the MJO performance hold in these model ensembles.

The symbiotic relation between the MJO and the higher-frequency CCEWs suggests that improved representation of one is likely accompanied by (or resulting from) better representation of the other in the climate models. Given that the MJO and CCEWs are the dominant modes on the intraseasonal and synoptic time scales respectively, efforts to improve the model representation of them as well as their interaction will lead to increased capability in forming a seamless prediction system from weather to climate (e.g., Waliser 2011; Moncrieff et al. 2012).

*Acknowledgments.* The authors thank three anonymous reviewers for their helpful comments on earlier versions of this paper. This work was supported by the Marine Meteorology Program of the Office of Naval Research under Project ONRBAA12-001, the NSF Climate and Large-Scale Dynamics Program under Awards AGS-1221013 and AGS-1228302, and the NOAA MAPP Program under Award NA12OAR4310075. The contribution from DEW to this study was performed on behalf of the Joint Institute for Regional Earth Science and Engineering (JIFRESSE) at the University of California, Los Angeles, and the Jet Propulsion Laboratory, California Institute of Technology, under a contract with the National Aeronautics and Space Administration.

## REFERENCES

Bao, Q., and Coauthors, 2013: The Flexible Global Ocean–Atmosphere–Land system model, spectral version 2: FGOALS-s2. *Adv. Atmos. Sci.,* **30,** 561–576, doi:10.1007/s00376-012-2113-9.

Benedict, J. J., and D. A. Randall, 2007: Observed characteristics of the MJO relative to maximum rainfall. *J. Atmos. Sci.,* **64,** 2332–2354, doi:10.1175/JAS3968.1.

Biello, J. A., and A. J. Majda, 2005: A new multiscale model for the Madden–Julian oscillation. *J. Atmos. Sci.,* **62,** 1694–1721, doi:10.1175/JAS3455.1.

Boberg, F., P. Berg, P. Thejll, W. J. Gutowski, and J. H. Christensen, 2009: Improved confidence in climate change projections of precipitation evaluated using daily statistics from the PRUDENCE ensemble. *Climate Dyn.,* **32,** 1097–1106, doi:10.1007/s00382-008-0446-y.

Côté, J., S. Gravel, A. Méthot, A. Patoine, M. Roch, and A. Staniforth, 1998: The operational CMC–MRB Global Environmental Multiscale (GEM) model. Part I: Design considerations and formulation. *Mon. Wea. Rev.,* **126,** 1373–1395, doi:10.1175/1520-0493(1998)126<1373:TOCMGE>2.0.CO;2.

Dai, A., 2006: Precipitation characteristics in eighteen coupled climate models. *J. Climate,* **19,** 4605–4630, doi:10.1175/JCLI3884.1.

Guo, Y., X. Jiang, and D. E. Waliser, 2014: Modulation of the convectively coupled Kelvin waves over South America and the tropical Atlantic Ocean in association with the Madden–Julian oscillation. *J. Atmos. Sci.,* **71,** 1371–1388, doi:10.1175/JAS-D-13-0215.1.

Haertel, P. T., and G. N. Kiladis, 2004: Dynamics of 2-day equatorial waves. *J. Atmos. Sci.,* **61,** 2707–2721, doi:10.1175/JAS3352.1.

Hazeleger, W., and Coauthors, 2012: EC-Earth V2.2: Description and validation of a new seamless earth system prediction model. *Climate Dyn.,* **39,** 2611–2629, doi:10.1007/s00382-011-1228-5.

Hendon, H. H., and B. Liebmann, 1994: Organization of convection within the Madden–Julian oscillation. *J. Geophys. Res.,* **99,** 8073–8084, doi:10.1029/94JD00045.

Hogan, T. F., and Coauthors, 2014: The Navy Global Environmental Model. *Oceanography,* **27,** 116–125, doi:10.5670/oceanog.2014.73.

Houze, R. A., Jr., 2004: Mesoscale convective systems. *Rev. Geophys.,* **42,** RG4003, doi:10.1029/2004RG000150.

——, S. S. Chen, D. E. Kingsmill, Y. Serra, and S. E. Yuter, 2000: Convection over the Pacific warm pool in relation to the atmospheric Kelvin–Rossby wave. *J. Atmos. Sci.,* **57,** 3058–3089, doi:10.1175/1520-0469(2000)057<3058:COTPWP>2.0.CO;2.

Huang, P., C. Chou, and R. Huang, 2013: The activity of convectively coupled equatorial waves in CMIP3 global climate models. *Theor. Appl. Climatol.,* **112,** 697–711, doi:10.1007/s00704-012-0761-4.

Huffman, G. J., and Coauthors, 2007: The TRMM Multisatellite Precipitation Analysis (TMPA): Quasi-global, multiyear, combined-sensor precipitation estimates at fine scales. *J. Hydrometeor.,* **8,** 38–55, doi:10.1175/JHM560.1.

Hung, M., J. Lin, W. Wang, D. Kim, T. Shinoda, and S. J. Weaver, 2013: MJO and convectively coupled equatorial waves simulated by CMIP5 climate models. *J. Climate,* **26,** 6185–6214, doi:10.1175/JCLI-D-12-00541.1.

Jiang, X., and Coauthors, 2015: Vertical structure and physical processes of the Madden-Julian Oscillation: Exploring key model physics in climate simulations. *J. Geophys. Res. Atmos.,* in press.

Khouider, B., and A. J. Majda, 2008a: Multicloud models for organized tropical convection: Enhanced congestus heating. *J. Atmos. Sci.,* **65,** 895–914, doi:10.1175/2007JAS2408.1.

——, and ——, 2008b: Equatorial convectively coupled waves in a simple multicloud model. *J. Atmos. Sci.,* **65,** 3376–3397, doi:10.1175/2008JAS2752.1.

——, Y. Han, A. J. Majda, and S. N. Stechmann, 2012: Multiscale waves in an MJO background and convective momentum transport feedback. *J. Atmos. Sci.,* **69,** 915–933, doi:10.1175/JAS-D-11-0152.1.

Kikuchi, K., and B. Wang, 2010: Spatiotemporal wavelet transform and the multiscale behavior of the Madden–Julian oscillation. *J. Climate,* **23,** 3814–3834, doi:10.1175/2010JCLI2693.1.

Kiladis, G., M. Wheeler, P. Haertel, K. Straub, and P. Roundy, 2009: Convectively coupled equatorial waves. *Rev. Geophys.,* **47,** RG2003, doi:10.1029/2008RG000266.

Kim, D., and Coauthors, 2009: Application of MJO simulation diagnostics to climate models. *J. Climate,* **22,** 6413–6436, doi:10.1175/2009JCLI3063.1.

——, A. H. Sobel, E. D. Maloney, D. M. W. Frierson, and I.-S. Kang, 2011: A systematic relationship between intraseasonal variability and mean state bias in AGCM simulations. *J. Climate,* **24,** 5506–5520, doi:10.1175/2011JCLI4177.1.

Klingaman, N. P., and Coauthors, 2015: Vertical structure and diabatic processes of the Madden–Julian oscillation: Linking hindcast fidelity to simulated diabatic heating and moistening. *J. Geophys. Res. Atmos.,* in press.

Lappen, C.-L., and C. Schumacher, 2012: Heating in the tropical atmosphere: What level of detail is critical for accurate MJO simulations in GCMs? *Climate Dyn.,* **39,** 2547–2568, doi:10.1007/s00382-012-1327-y.

Lau, W. K. M., and D. E. Waliser, Eds., 2005: *Intraseasonal Variability of the Atmosphere–Ocean Climate System.* Springer, 474 pp.

Lin, J.-L., and Coauthors, 2006: Tropical intraseasonal variability in 14 IPCC AR4 climate models. Part I: Convective signals. *J. Climate,* **19,** 2665–2690, doi:10.1175/JCLI3735.1.

Liou, C. S., and Coauthors, 1997: The second-generation global forecast system at the Central Weather Bureau in Taiwan. *Wea. Forecasting,* **12,** 653–663, doi:10.1175/1520-0434-12.3.653.

Liu, F., and B. Wang, 2012: Impacts of upscale heat and momentum transfer by moist Kelvin waves on the Madden–Julian oscillation: A theoretical model study. *Climate Dyn.,* **40,** 213–224, doi:10.1007/s00382-011-1281-0.

Madden, R., and P. Julian, 1971: Detection of a 40–50 day oscillation in the zonal wind in the tropical Pacific. *J. Atmos. Sci.,* **28,** 702–708, doi:10.1175/1520-0469(1971)028<0702:DOADOI>2.0.CO;2.

——, and ——, 1972: Description of global-scale circulation cells in the tropics with a 40–50 day period. *J. Atmos. Sci.,* **29,** 1109–1123, doi:10.1175/1520-0469(1972)029<1109:DOGSCC>2.0.CO;2.

Majda, A. J., 2007: New multiscale models and self-similarity in tropical convection. *J. Atmos. Sci.,* **64,** 1393–1404, doi:10.1175/JAS3880.1.

——, and R. Klein, 2003: Systematic multiscale models for the tropics. *J. Atmos. Sci.,* **60,** 393–408, doi:10.1175/1520-0469(2003)060<0393:SMMFTT>2.0.CO;2.

——, and J. A. Biello, 2004: A multiscale model for tropical intraseasonal oscillations. *Proc. Natl. Acad. Sci. USA,* **101,** 4736–4741, doi:10.1073/pnas.0401034101.

——, and S. N. Stechmann, 2009: A simple dynamical model with features of convective momentum transport. *J. Atmos. Sci.,* **66,** 373–392, doi:10.1175/2008JAS2805.1.

Masunaga, H., T. L'Ecuyer, and C. Kummerow, 2006: The Madden–Julian oscillation recorded in early observations from the Tropical Rainfall Measuring Mission (TRMM). *J. Atmos. Sci.,* **63,** 2777–2794, doi:10.1175/JAS3783.1.

Matsuno, T., 1966: Quasi-geostrophic motions in the equatorial area. *J. Meteor. Soc. Japan,* **44,** 25–43.

Merryfield, W. J., and Coauthors, 2013: The Canadian Seasonal to Interannual Prediction System. Part I: Models and initialization. *Mon. Wea. Rev.,* **141,** 2910–2945, doi:10.1175/MWR-D-12-00216.1.

Molod, A., L. Takacs, L. M. Suarez, J. Bacmeister, I.-S. Song, and A. Eichmann, 2012: The GEOS-5 atmospheric general circulation model: Mean climate and development from MERRA to Fortuna. NASA TM-2012-104606, NASA Tech. Rep. Series on Global Modeling and Data Assimilation, Vol. 28, 117 pp.

Moncrieff, M. W., 2004: Analytic representation of the large-scale organization of tropical convection. *J. Atmos. Sci.,* **61,** 1521–1538, doi:10.1175/1520-0469(2004)061<1521:AROTLO>2.0.CO;2.

——, D. E. Waliser, M. J. Miller, M. A. Shapiro, G. R. Asrar, and J. Caughey, 2012: Multiscale convective organization and the YOTC virtual global field campaign. *Bull. Amer. Meteor. Soc.,* **93,** 1171–1187, doi:10.1175/BAMS-D-11-00233.1.

Nakazawa, T., 1988: Tropical super clusters within intraseasonal variations over the western Pacific. *J. Meteor. Soc. Japan,* **66,** 823–836.

Neale, R. B., and Coauthors, 2012: Description of the NCAR Community Atmosphere Model: CAM 5.0. NCAR Tech. Rep. NCAR/TN–486+STR, 274 pp. [Available online at http://www.cesm.ucar.edu/models/cesm1.0/cam/docs/description/cam5_desc.pdf.]

Petch, J., D. Waliser, X. Jiang, P. Xavier, and S. Woolnough, 2011: A global model intercomparison of the physical processes associated with the MJO. *GEWEX News,* Vol. 21, No. 3, International GEWEX Project Office, Silver Spring, MD, 3–5.

Roundy, P. E., 2008: Analysis of convectively coupled Kelvin waves in the Indian Ocean MJO. *J. Atmos. Sci.,* **65,** 1342–1359, doi:10.1175/2007JAS2345.1.

——, and W. M. Frank, 2004: A climatology of waves in the equatorial region. *J. Atmos. Sci.,* **61,** 2105–2132, doi:10.1175/1520-0469(2004)061<2105:ACOWIT>2.0.CO;2.

Saha, S., and Coauthors, 2006: The NCEP Climate Forecast System. *J. Climate,* **19,** 3483–3517, doi:10.1175/JCLI3812.1.

——, and Coauthors, 2014: The NCEP Climate Forecast System version 2. *J. Climate,* **27,** 2185–2208, doi:10.1175/JCLI-D-12-00823.1.

Schmidt, G. A., and Coauthors, 2014: Configuration and assessment of the GISS ModelE2 contributions to the CMIP5 archive. *J. Adv. Model. Earth Syst.,* **6,** 141–184, doi:10.1002/2013MS000265.

Schubert, S., R. Dole, H. Van den Dool, M. Suarez, and D. Waliser, 2002: Prospects for improved forecasts of weather and short-term climate variability on subseasonal (2 week to 2 month) time scales. NASA/TM–2002–104606, Tech. Rep. Series on Global Modeling and Data Assimilation, Vol. 23, Goddard Space Flight Center, 171 pp. [Available online at http://gmao.gsfc.nasa.gov/pubs/tm/docs/Schubert140.pdf.]

Slingo, J. M., and Coauthors, 1996: Intraseasonal oscillations in 15 atmospheric general circulation models: Results from an AMIP diagnostic subproject. *Climate Dyn.,* **12,** 325–357, doi:10.1007/BF00231106.

Sobel, A. H., and E. D. Maloney, 2013: Moisture modes and the eastward propagation of the MJO. *J. Atmos. Sci.,* **70,** 187–192, doi:10.1175/JAS-D-12-0189.1.

Song, X., and G. J. Zhang, 2011: Microphysics parameterization for convective clouds in a global climate model: Description and single-column model tests. *J. Geophys. Res.,* **116,** D02201, doi:10.1029/2010JD014833.

Sperber, K. R., and H. Annamalai, 2008: Coupled model simulations of boreal summer intraseasonal (30–50 day) variability, Part 1: Systematic errors and caution on use of metrics. *Climate Dyn.,* **31,** 345–372, doi:10.1007/s00382-008-0367-9.

——, J. M. Slingo, D. E. Waliser, and P. M. Inness, 2008: Coarse-resolution models only partly cloudy. *Science,* **320,** 612–612, doi:10.1126/science.320.5876.612a.

Stan, C., M. Khairoutdinov, C. A. DeMott, V. Krishnamurthy, D. M. Straus, D. A. Randall, J. L. Kinter, and J. Shukla, 2010: An ocean–atmosphere climate simulation with an embedded cloud resolving model. *Geophys. Res. Lett.,* **37,** L01702, doi:10.1029/2009GL040822.

Stevens, B., and Coauthors, 2013: Atmospheric component of the MPI-M Earth System Model: ECHAM6. *J. Adv. Model. Earth Syst.,* **5,** 146–172, doi:10.1002/jame.20015.

Straub, K. H., and G. N. Kiladis, 2003: Interactions between the boreal summer intraseasonal oscillation and higher-frequency tropical wave activity. *Mon. Wea. Rev.,* **131,** 945–960, doi:10.1175/1520-0493(2003)131<0945:IBTBSI>2.0.CO;2.

——, P. T. Haertel, and G. N. Kiladis, 2010: An analysis of convectively coupled Kelvin waves in 20 WCRP CMIP3 global coupled climate models. *J. Climate,* **23,** 3031–3056, doi:10.1175/2009JCLI3422.1.

Takayabu, Y. N., 1994: Large-scale cloud disturbances associated with equatorial waves. Part I: Spectral features of the cloud disturbances. *J. Meteor. Soc. Japan,* **72,** 433–448.

Tsuang, B.-J., C.-Y. Tu, and K. Arpe, 2001: Lake parameterization for climate models. Max Planck Institute for Meteorology Rep. 316, Hamburg, Germany, 72 pp.

Voldoire, A., and Coauthors, 2013: The CNRM-CM5.1 global climate model: Description and basic evaluation. *Climate Dyn.,* **40,** 2091–2121, doi:10.1007/s00382-011-1259-y.

Waliser, D. E., 2006: Intraseasonal variations. *The Asian Monsoon,* B. Wang, Ed., Springer, 203–257.

——, 2011: Predictability and forecasting. *Intraseasonal Variability of the Atmosphere–Ocean Climate System,* 2nd ed., W. K. M. Lau and D. E. Waliser, Eds., Springer, 433–476.

——, K. M. Lau, W. Stern, and C. Jones, 2003: Potential predictability of the Madden–Julian oscillation. *Bull. Amer. Meteor. Soc.,* **84,** 33–50, doi:10.1175/BAMS-84-1-33.

——, and Coauthors, 2012: The "year" of tropical convection (May 2008–April 2010): Climate variability and weather highlights. *Bull. Amer. Meteor. Soc.,* **93,** 1189–1218, doi:10.1175/2011BAMS3095.1.

Walters, D. N., and Coauthors, 2011: The Met Office Unified Model global atmosphere 3.0/3.1 and JULES global land 3.0/3.1 configurations. *Geosci. Model Dev.,* **4,** 919–941, doi:10.5194/gmd-4-919-2011.

Wang, B., 2005: Theory. *Intraseasonal Variability in the Atmosphere–Ocean Climate System,* W. K. M. Lau and D. E. Waliser, Eds., Praxis, 307–360.

——, and F. Liu, 2011: A model for scale interaction in the Madden–Julian Oscillation. *J. Atmos. Sci.,* **68,** 2524–2536, doi:10.1175/2011JAS3660.1.

Watanabe, M., and Coauthors, 2010: Improved climate simulation by MIROC5: Mean states, variability, and climate sensitivity. *J. Climate,* **23,** 6312–6335, doi:10.1175/2010JCLI3679.1.

Weaver, S. J., W. Wang, M. Chen, and A. Kumar, 2011: Representation of MJO variability in the NCEP Climate Forecast System. *J. Climate,* **24,** 4676–4694, doi:10.1175/2011JCLI4188.1.

Wheeler, M., and G. N. Kiladis, 1999: Convectively coupled equatorial waves: Analysis of clouds and temperature in the wavenumber–frequency domain. *J. Atmos. Sci.,* **56,** 374–399, doi:10.1175/1520-0469(1999)056<0374:CCEWAO>2.0.CO;2.

Wu, T., and Coauthors, 2010: The Beijing Climate Center atmospheric general circulation model: Description and its performance for the present-day climate. *Climate Dyn.,* **34,** 123–147, doi:10.1007/s00382-008-0487-2.

Wu, X., and L. Deng, 2013: Comparison of moist static energy and budget between the GCM simulated Madden–Julian oscillation and observations over the Indian Ocean and western Pacific. *J. Climate,* **26,** 4981–4993, doi:10.1175/JCLI-D-12-00607.1.

Xavier, P., and Coauthors, 2015: Vertical structure and diabatic processes of the Madden-Julian Oscillation: Biases and uncertainties at short range. *J. Geophys. Res. Atmos.,* in press.

Yang, G.-Y., B. Hoskins, and J. Slingo, 2007: Convectively coupled equatorial waves. Part I: Horizontal and vertical structures. *J. Atmos. Sci.,* **64,** 3406–3423, doi:10.1175/JAS4017.1.

——, J. Slingo, and B. Hoskins, 2009: Convectively coupled equatorial waves in high-resolution Hadley Centre climate models. *J. Climate,* **22,** 1897–1919, doi:10.1175/2008JCLI2630.1.

Yukimoto, S., and Coauthors, 2012: A new global climate model of the Meteorological Research Institute: MRI-CGCM3—Model description and basic performance. *J. Meteor. Soc. Japan,* **90A,** 23–64.

Zhang, C., 2005: Madden–Julian oscillation. *Rev. Geophys.,* **43,** RG2003, doi:10.1029/2004RG000158.

——, M. Dong, S. Gualdi, H. H. Hendon, E. D. Maloney, A. Marshall, K. R. Sperber, and W. Wang, 2006: Simulations of the Madden–Julian oscillation in four pairs of coupled and uncoupled global models. *Climate Dyn.,* **27,** 573–592, doi:10.1007/s00382-006-0148-2.

Zhang, G. J., and M. Mu, 2005: Simulation of the Madden–Julian oscillation in the NCAR CCM3 using a revised Zhang–McFarlane convection parameterization scheme. *J. Climate,* **18,** 4046–4064, doi:10.1175/JCLI3508.1.

Zhu, H., H. Hendon, M. Dix, Z. Sun, G. Dietachmayer, and K. Puri, 2013: Vertical structure and diabatic processes of the MJO. A Global Model Inter-comparison Project: Preliminary results from ACCESS model. CAWCR Research Letters, Issue 10, Centre for Australian Weather and Climate Research, Melbourne, VIC, Australia, 2034–2038. [Available online at http://www.cawcr.gov.au/publications/researchletters/CAWCR_Research_Letters_10.pdf.]

Zuluaga, M. D., and R. A. Houze Jr., 2013: Evolution of the population of precipitating convective systems over the equatorial Indian Ocean in active phases of the Madden–Julian oscillation. *J. Atmos. Sci.,* **70,** 2713–2725, doi:10.1175/JAS-D-12-0311.1.